Three-Dimensional Numerical Modelling of Wave-Induced Scour Around Piles in a Side-by-Side Arrangement

Nadeem Ahmad *, Hans Bihs, Dag Myrhaug, Arun Kamath and Øivind A. Arntsen
Department of Civil and Environmental Engineering, Norwegian University of Science and Technology (NTNU), 7491 Trondheim, Norway

Coastal Engineering, 2018, **138** , pp. 132-151.
DOI: http://dx.doi.org/10.1016/j.coastaleng.2018.04.016

Abstract

The paper presents the numerical modelling of wave-induced scour around piles in a side-by-side arrangement using the open-source CFD model REEF3D. The model solves the Reynolds-Averaged Navier-Stokes equations to calculate wave hydrodynamics. The turbulence under the wave action is calculated using the k-ω model. The free surface is captured with the level set method. The simulated flow field is coupled with the morphological module in REEF3D to simulate the scouring process. The morphological evolution of the sediment bed is based on the Exner formula. For a more realistic calculation of bed scouring and deposition, the modified critical bed shear stress on a sloping bed together with a sand slide algorithm is implemented in the morphological model. First, the model is tested for numerical modelling of wave-induced scour around a single pile. The study presents wave generation and the scouring process in a full-sized and a reduced-length numerical wave tank (NWT) using the relaxation and the active wave absorption method. Furthermore, a discussion on the partial temporal decoupling for the time scales of the morphological and the hydrodynamic models is made. The simulated result shows that the fully developed waves and resulting scouring can be modelled in a reduced-length NWT with the same quality as seen for a full-sized NWT. The validated model is then used to simulate the wave-induced scour around piles in a side-by-side arrangement. The capacity of the model to simulate wave-induced scour in the gap between two piles along with the free surface is demonstrated. The results show the variation of the normalised maximum scour depth S/D with the gap ratios G/D and the Keulegan-Carpenter number. The formation of the jet effect between the piles with different G/D values is also discussed.

*Corresponding author, nadeem.ahmad@ntnu.no

Keywords: Wave-induced scour; Piles in a side-by-side arrangement; Relaxation and AWA method; Reduced-length NWT; Gap ratio; Free surface

1 Introduction

Piles in a group are commonly used to support marine structures. The arrangement of piles is chosen in such a way that it offers high structural integrity against wave action. But on the other hand, the arrangement of piles alters the wave hydrodynamics. The alteration occurs in the form of flow contraction and turbulent vortices around the piles. Consequently, this results in an increased bed shear stress which leads to scour. This can be a threat to the structural stability of the piles, especially under storm conditions when the wave flow characteristics change drastically and develop rapid scouring. Therefore, the wave-induced scour around a group of piles needs to be analysed thoroughly.

The scour under waves and steady flow around a single pile has received a lot of attention in the past decades e.g. (Sumer et al., 1992; Whitehouse, 1998; Melville and Coleman, 2000; Sumer and Fredsøe, 2001; Nielsen et al., 2012). These studies discussed the change in hydrodynamics around a pile in terms of pressure, velocity and the development of horseshoe vortices. The effect of these changes were linked to an increase in bed shear stress which results in increased scour around the cylinder. In addition, the influence of other parameters such as the Keulegan-Carpenter (KC) number, the Shields parameter, sediment grading, the geometric shape of the cylinder and the effect of flow alignment were also discussed. Results were presented for the maximum scour depth and the temporal variation of the scouring process.

The scouring process around a group of piles is more complex compared to scouring around a single pile. There is a considerable amount of literature which specifically investigate the process experimentally. Chow and Herbich (1978) investigated the wave-induced scouring process around a group of cylindrical piles. In their study, the effect of the gap ratio (G/D), where G is the spacing between two individual piles and D is the diameter of the cylindrical pile, was investigated. It was found that G/D is a critical parameter affecting the equilibrium scour. However, the influence of the KC number for different G/D was not investigated. Sumer and Fredsøe (1998) conducted further tests to elaborate on this issue. The study focused on the effect of the KC number and G/D on the wave-induced scour. They concluded that the normalised maximum scour depth (S/D), where S is the equilibrium scour depth, varies with the G/D and KC number. Bayram and Larson (2000) carried out a field study on wave-induced scour around multiple piles. They analysed a 200 m long beach profile with a group of piles on the coast of Japan and found that the KC number is the prime

Postprint, published in Coastal Engineering, doi:http://dx.doi.org/10.1016/j.coastaleng.2018.04.016

factor governing wave-induced scour, also observing that the extent of the scour around the individual piles overlaps even in case of $G/D > 4$. This result contradicts the experimental observations made by Sumer and Fredsøe (1998) which suggest that piles in a side-by-side arrangement for $G/D > 2$ act as individual piles, showing two very distinct scour holes. In addition, Bayram and Larson (2000) discussed only the final scour depth with no discussion of the hydrodynamics between the two piles. Posey (1961) reported through their experimental observations that the combined wave-current action might form a single scour hole around a group of piles, while the waves alone would develop a distinct scour hole around the individual piles for large G/D. Therefore, a further investigation of the hydrodynamics and resulting normalised maximum scour depth (S/D) as G/D and KC increase can be used to improve the understanding of scour problems for piles in a side-by-side arrangement.

Numerical modelling of the hydrodynamics and the resulting scour is a challenging task and carried out by many researchers, e.g. (Olsen and Melaaen, 1993; Olsen and Kjellesvig, 1998; Richardson and Panchang, 1998). In these studies, three-dimensional steady flow around a vertical cylinder is calculated by solving the Navier-Stokes equations. The simulated steady flow field is coupled with morphological calculations to simulate clear-water scour. Tseng et al. (2000) investigated the three-dimensional turbulent steady flow field around a square and a circular pier. The results of the flow simulation were presented for the horseshoe and wake vortices impacting the scour mechanism. Roulund et al. (2005) carried out a similar study to investigate live-bed scour. In their study, the numerical model solved the three-dimensional steady-state flow around a single cylinder. The simulated flow field is coupled with a morphological model to evaluate the scouring process for non-cohesive sediments. Based on the simulated results for the flow field and the bed shear stress calculations, it was concluded that the bed shear stress around the cylinder reduces as the scour hole develops. However, the model did not solve the free surface which limited the study to cases of lower Froude numbers ($Fr < 0.2$). Liu and Garcia (2008) investigated numerically the scour process around a single pile with free surface calculation. The volume-of-fluid (VOF) method is used for the free surface capturing and the bed deformation is captured with the moving-mesh method. The scour process is modelled with a quasi-steady approach. The study discussed the scour around a single cylinder under waves with a low KC = 1.1. Bihs and Olsen (2011) discussed local scour around an abutment under steady current and found that the reduction of the bed shear stress on a sloping bed improves the results of the numerical simulations significantly. The Kovacs and Parker (1994) formula was found to be the most suitable approach for the scour calculation on a sloping bed. Afzal et al. (2015) investigated the local scour around a single cylinder under waves and current using the open-source CFD model REEF3D. The simulated results for both waves and current showed good agreement with experimental observations. Ahmad et al. (2015) presented numerical results for local scour around a non-slender cylinder for a lower range of KC ≤ 1.2, using the same numerical

model. The results correlate fairly well with the experimental data, which suggests that the scour depth and sediment deposition increases with the KC number. Baykal et al. (2015) numerically investigated the scour around a vertical pile under steady current and found that the calculated scour depth is reduced by 50% when the suspended load is not accounted for. Baykal et al. (2017) studied the significance of the wave condition on the equilibrium scour depth and showed promising results for the backfilling of the scour hole under the wave action.

However, the modelling of wave-induced scour around a group of cylinders is investigated by few researchers. Myrhaug and Rue (2005) studied scour around a group of piles in random waves. The formulation for normalised maximum scour depth S/D by Sumer and Fredsøe (1998) is coupled with random waves to calculate the scour depths through a stochastic approach. The studies about numerical modelling of scour have focused on the local scour around a single pile. However, it is equally important to understand the scouring process around a group of piles with the effect of variable spacing between piles and different wave conditions.

In this paper, the three-dimensional numerical modelling of scour around the piles in a side-by-side arrangement is analysed. The paper discusses and compares the wave generation and the wave-induced scour calculation in a full-sized and the reduced-length numerical wave tank (NWT). The partial temporal decoupling for the time scales of the morphological and hydrodynamic model is studied to reduce the large computational time involved in the scouring process calculations. The model is validated by comparing the computed temporal variation of the scouring process and the equilibrium scour depth with the experimental data (Sumer et al., 1992). The validated model is then used to evaluate the wave hydrodynamics and the resulting scour around the piles in a side-by-side arrangement. The study investigates the wave-induced jet effect in the gap between two piles and the resulting scour due to the change in the G/D ratio and the KC number. The numerical results are compared with experimental observations (Sumer and Fredsøe, 1998). The temporal variation of the scouring process, normalised maximum scour depth (S/D) and the scour extent around piles are studied to gain more knowledge about the scouring around the piles in a side-by-side arrangement.

2 Numerical Model

2.1 Hydrodynamic model

The open-source CFD model REEF3D (Bihs et al., 2016) is used for the numerical modelling of the wave hydrodynamics and the sediment transport. The model has been successfully used for the numerical modelling of breaking waves (Alagan Chella et al., 2016), simulation of floating bodies (Bihs and Kamath, 2017) and interaction of breaking waves with a vertical cylinder (Kamath et al., 2016). It solves the incompressible Reynolds-Averaged Navier-Stokes (RANS) equations, along with the continuity equation to calculate the velocity field in the

NWT. The continuity and momentum equations are shown below:

$$\frac{\partial u_i}{\partial x_i} = 0 \tag{1}$$

$$\frac{\partial u_i}{\partial t} + u_j \frac{\partial u_i}{\partial x_j} = -\frac{1}{\rho}\frac{\partial p}{\partial x_i} + \frac{\partial}{\partial x_j}\left[(\nu + \nu_t)\left(\frac{\partial u_i}{\partial x_j} + \frac{\partial u_j}{\partial x_i}\right)\right] + g_i \tag{2}$$

where u_i is the velocity, p is the pressure, ρ is the fluid density, ν is the fluid kinematic viscosity, ν_t is the eddy viscosity and g is the gravitational acceleration.

2.2 Turbulence model

The k-ω model (Wilcox, 1994) is used to calculate the eddy-viscosity by solving for the turbulent kinetic energy k and the specific turbulent dissipation ω:

$$\frac{\partial k}{\partial t} + u_j \frac{\partial k}{\partial x_j} = \frac{\partial}{\partial x_j}\left[\left(\nu + \frac{\nu_t}{\sigma_k}\right)\frac{\partial k}{\partial x_j}\right] + P_k - \beta_k k\omega \tag{3}$$

$$\frac{\partial \omega}{\partial t} + u_j \frac{\partial \omega}{\partial x_j} = \frac{\partial}{\partial x_j}\left[\left(\nu + \frac{\nu_t}{\sigma_\omega}\right)\frac{\partial \omega}{\partial x_j}\right] + \frac{\omega}{k}\alpha P_k - \beta\omega^2 \tag{4}$$

where P_k is the turbulent production rate and is defined as follows:

$$P_k = \nu_t \frac{\partial u_i}{\partial x_j}\left[\frac{\partial u_i}{\partial x_j} + \frac{\partial u_j}{\partial x_i}\right] \tag{5}$$

The other closure coefficients are α=$\frac{5}{9}$, $\beta_k = \frac{9}{100}$, β=$\frac{3}{40}$, $\sigma_\omega = 2$ and $\sigma_k = 2$. The over-production of the turbulence in highly strained flow associated with the oscillatory fluid motion under waves outside the boundary layer is prevented by limiting the eddy-viscosity (Durbin, 2009) as follows:

$$\nu_t = \min\left(\frac{k}{\omega}, \sqrt{\frac{2}{3}}\frac{k}{|\mathbf{S}|}\right) \tag{6}$$

where $\mathbf{S}$ is the mean rate of strain.

2.3 Free surface model

The free surface is captured using the level set method (Osher and Sethian, 1988). This method uses a continuous signed distance function $\phi(\vec{x}, t)$ to represent the interface between two immiscible fluids. The interface is computed under a velocity field u_j. The level set function is calculated as zero on the interface, positive for phase 1 and negative for phase 2.

This is defined as follows:

$$\phi(\vec{x},t)\begin{cases} > 0 & if\ \vec{x}\ is\ in\ phase\ 1 \\ = 0 & if\ \vec{x}\ is\ at\ the\ interface \\ < 0 & if\ \vec{x}\ is\ in\ phase\ 2 \end{cases} \tag{7}$$

The velocity field u_j is calculated from the solution of the RANS-equations and convects the level set function in space and time as follows:

$$\frac{\partial \phi}{\partial t} + u_j \frac{\partial \phi}{\partial x_j} = 0 \tag{8}$$

As the free surface evolves, the level set function $\phi(\vec{x},t)$ loses its signed distance property. Therefore, the level set function $\phi(\vec{x},t)$ is reinitialised at each time step (Peng et al., 1999).

2.4 Numerical wave generation and absorption

The wave generation in the NWT is managed with the relaxation method (Jacobsen et al., 2012) and the active wave absorption (AWA) method (Schäffer and Klopman, 2000). The study discusses and compares the quality of waves and resulting sediment transport in a full-sized and reduced-length NWT. For a full-sized NWT, waves are generated with the relaxation method. In this method, wave generation takes place in a relaxation zone of one wavelength. Fifth-order cnoidal waves are generated by prescribing the wave elevation (η) with the horizontal and vertical velocity in the wave generation zone. The computational values of wave velocity and elevation from the inlet are transformed to the analytical values over relaxation zone using the relaxation function $\Gamma(x)$, which is defined as follows:

$$\Gamma(x) = 1 - \frac{exp(x^{3.5}) - 1}{exp(1) - 1} \tag{9}$$

and is applied inside the relaxation domain as follows:

$$(u,\phi) = \Gamma(x)(u,\phi)_{computed} + [1 - \Gamma(x)](u,\phi)_{target} \tag{10}$$

where x is the length scale which varies from 0 to 1 in order to transform the still water depth at the inlet to waves over the relaxation zone. The waves are absorbed with the AWA method. In this method, the waves reaching the outlet are absorbed by cancelling out the reflected waves based on shallow water theory and prescribing the velocity u_c as follows:

$$u_c = -\sqrt{\frac{g}{h}}\ \eta_r \tag{11}$$

where η_r is the reflected wave amplitude which is defined as:

$$\eta_r = \eta_m - h \tag{12}$$

Here η_m is the actual free surface elevation and h is the still water level. Thus the reflected waves from the outlet are prevented without disturbing the incident waves approaching the pile in the NWT. However, for a reduced-length NWT, both the wave generation and the absorption are managed with the AWA method.

2.5 Numerical schemes and solver

The model approximates spatial derivatives using advanced finite difference methods on a Cartesian grid, where the convective terms of the momentum equations are discretized with the fifth-order accurate conservative Weighted Essential Non-Oscillatory (WENO) scheme (Jiang and Shu, 1996). The convective terms of the turbulence model and the level set function are discretized with the Hamilton-Jacobi formulation of the WENO scheme (Jiang and Peng, 2000). A third-order TVD Runge-Kutta time scheme (Shu and Osher, 1988) is used for time treatment of the momentum equations, the level set function and the reinitialisation equations. The hydrodynamic time step for the transient flow field is determined using adaptive time stepping in order to maintain an optimal time step. Here, the time step is controlled using the Courant-Friederichs-Lewy (CFL) number (Griebel et al., 1998), which takes into account the influence of the velocity, diffusion, and source terms such as the gravity. In a RANS model, the diffusion criterion can become restrictive and therefore, it is treated implicitly to remove it from the CFL criterion (Bihs et al., 2016). The pressure is treated with the projection method (Chorin, 1968). The BiCGStab (Vorst, 1992) solver from the high-performance solver package HYPRE with the semi-coarsening multi-grid preconditioner PFMG (Ashby and Flagout, 1996) is implemented to solve the Poisson equation for the pressure. An immersed boundary method with the local directional ghost cell approach (Berthelsen and Faltinsen, 2008), adapted to three dimensions, is used to define boundary conditions for complex geometries.

2.6 Morphological model

Sediment transport is calculated based on the flow field simulated by the hydrodynamic module in REEF3D. The bed shear stress is determined considering a logarithmic velocity profile near the sediment bed. The bed shear stress τ is defined as follows:

$$\tau = \rho u_*^2 \tag{13}$$

where u_* is the shear velocity defined as:

$$u_* = \frac{u}{\frac{1}{\kappa}\ ln\left(\frac{30z}{k_s}\right)} \tag{14}$$

Here u is the velocity at a height z above the bed, $\kappa = 0.4$ is the von Karman constant, $k_s = 3d_{50}$ is the equivalent sand roughness and d_{50} is the median grain size.
The bed-load calculations are made with the formulation proposed by van Rijn (1984a). It is based on the sediment particle mobility which suggests that when the bed shear stress just exceeds the critical bed shear stress, the motion of the particles is initiated. The formula for the bed-load transport rate incorporates two dimensionless parameters, the transport stage parameter $T = (\tau - \tau_{cr})/\tau_{cr}$ and the particle parameter D_* which is defined as follows:

$$D_* = d_{50}\left[\frac{(s-1)g}{\nu^2}\right]^{1/3} \tag{15}$$

where τ_{cr} is the modified Shields critical bed shear stress (Eq. 20), $s = \rho_s/\rho$ is the specific density, ρ_s is the sediment density and ρ is the water density. The bed-load transport rate $q_{b,i}$ is then (van Rijn, 1984a):

$$\frac{q_{b,i}}{d_{50}^{1.5}\sqrt{(s-1)g}} = 0.053\ \frac{T^{2.1}}{D_*^{0.3}} \tag{16}$$

The suspended sediment load is calculated using a convection-diffusion equation. The numerical treatment for this transport equation is performed in a similar fashion as for the momentum equations.

$$\frac{\partial c}{\partial t} + u_j\frac{\partial c}{\partial x_j} + w_s\frac{\partial c}{\partial z} = \frac{\partial}{\partial x_j}\left(\Gamma\frac{\partial c}{\partial x_j}\right) \tag{17}$$

where c is the suspended load concentration, w_s is the fall velocity of the sediment particles and Γ is the sediment mixing coefficient. The value of Γ is assumed to be equal to the eddy viscosity (Hunt, 1954). The solution of this equation is based on the boundary conditions as the zero vertical sediment flux at the free surface and the bottom suspended load concentration (c_b), beside the nearest grid to the bed, is calculated from van Rijn (1984b) formula:

$$c_b = 0.015\frac{d_{50}}{a}\left(\frac{T^{1.5}}{D_*^{0.3}}\right) \tag{18}$$

where a is the reference level for the suspended load. In the present model, the reference level is assumed to be equal to the equivalent-roughness height as $k_s = 3d_{50}$. The sediment

concentration close to the bed is interpolated using Rouse (1937) equation as:

$$c(z) = c_b \left(\frac{h-z}{z} \frac{a}{h-a} \right)^z \tag{19}$$

where z is distance from middle of the grid nearest to the bed (Olsen, 2003).

The approach to calculate the critical bed shear stress (τ_0) using the Shields graph is valid for a horizontal bed under a unidirectional flow. However, during the formation of the scour hole, the bed profile changes with longitudinal and transverse sloping beds. Therefore, it becomes important to account for the effect of the sloping bed into the calculation of the critical bed shear stress that is considered to be the prime factor responsible for the the incipient motion of sediment particles. Thus, in the present morphological model, a modified critical bed shear stress (τ_{cr}) on a sloping bed is calculated using the formulation by Dey (2003):

$$\tau_{cr} = \widetilde{\tau}\ \tau_0 \tag{20}$$

where τ_0 is the critical bed shear stress on a horizontal bed and $\widetilde{\tau}$ is the critical bed shear stress ratio to account for the effect of the sloping bed by considering the longitudinal bed slope θ, the transverse bed slope α, the angle of repose of the sediment φ and the drag and lift forces, yielding the following expression for the critical shear stress ratio $\widetilde{\tau}$ as:

$$\begin{aligned} \widetilde{\tau} = \frac{1}{\big(1-\eta\tan\varphi\big)\tan\varphi} \Big\{ &-\big(\sin\theta + \eta\tan^2\varphi\sqrt{\cos^2\theta - \sin^2\alpha}\big) \\ &+ \big[\big(\sin\theta + \eta\tan^2\varphi\sqrt{\cos^2\theta - \sin^2\alpha}\ \big)^2 \\ &+ \big(1-\eta^2\tan^2\varphi\big)\big(\cos^2\theta\tan^2\varphi - \sin^2\alpha\tan^2\varphi - \sin^2\theta - \sin^2\alpha\big)\big]^{0.5} \Big\} \end{aligned} \tag{21}$$

where η is the ratio of the drag force to the inertia force. Details of the formula and the definition sketch of forces acting on a particle lying on a combined transverse and longitudinal sloping bed can be found in Dey (2003) and Bihs and Olsen (2011). Generally, the critical shear stress ratio on a transverse sloping bed will be $\widetilde{\tau} \leq 1$. This means a reduction in the critical bed shear stress on a transverse sloping bed for all values of α. However, the critical bed shear stress ratio on the longitudinal sloping bed depends on type of the slope. A downhill sloping bed results in $\widetilde{\tau} \leq 1$ and an uphill sloping bed yields $\widetilde{\tau} \geq 1$. Thus, a decrease in the magnitude of the critical shear stress on a downhill and an increase on an uphill sloping bed. The sand slide algorithm (Burkow and Griebel, 2016) is implemented in the morphological model to account for the process of the excess sediment slump down when the bed slope exceeds the angle of repose (φ). The algorithm acts as a slope limiter and is implemented by applying a correction of -2° to the bed slope exceeding the angle of repose φ, as suggested by Roulund et al. (2005). As seen, the downhill bed slope is expected to be larger than the uphill bed slope (Sumer and Fredsøe, 2002). Therefore, for this study, the modified angle of

repose for the downhill slope is assumed to be $\varphi = 45°$, and for the uphill bed slope, $\varphi = 35°$, depending on the bed velocity vector orientation relative to the bed slope, as suggested by Lysne (1970).

The change in bed elevation is calculated with Exner's formula, based on the conservation of sediment mass where the horizontal spatial variation in the bed-load is conserved with the spatial change in the vertical bed elevation. The morphological evolution occurs as a non-linear propagation of the bed-level deformation in the direction of the sediment transport. The transient change in bed level is defined as follows:

$$\frac{\partial z_b}{\partial t} + \frac{1}{(1-n)} \left[\frac{\partial q_{b,x}}{\partial x} + \frac{\partial q_{b,y}}{\partial y} \right] + E - D = 0 \tag{22}$$

where z is the bed-level, $q_{b,x}$ and $q_{b,y}$ are the bed-load in x and y-direction, respectively, at the morphological time step, E is the sediment entrainment rate from the bed-load to the suspended-load, D is the sediment deposition rate from the suspended-load onto the bed. The term $(E - D)$ defines the net flux of sediment across the interface between the bed-load and suspended-load and is calculated as suggested by Wu et al. (2000).

The sediment bed is modelled with the level set method approach which is an implicit representation of the sediment bed as the zero level set. The driving velocity $F = \partial z_b/\partial t$ (Eq. 21) moves the interface in the vertical direction to represent the change in the sediment bed due to the scouring action. The main advantage of this approach is the consistency and numerical stability of the morphological evolution which does not require re-meshing.

3 Numerical setup and model validation

In this section, the numerical results for the model validation are presented. First, the grid convergence study in a full-sized NWT and the wave generation in a reduced-length NWT are discussed. Then, the accuracy of the wave-induced scour calculation in a full-sized and a reduced-length NWT are tested and compared. Finally, the numerical results for the partial temporal decoupling of the time scales for the morphological and hydrodynamic models are presented. The details of the tests carried out for the validation are listed in Table 1.

The computational setup for the model validation is the same as the one employed by Sumer et al. (1992). It is a 28.0 m long, 2.0 m wide and 1.0 m high flume with a pile of diameter $D = 0.10$ m fixed in the center as shown in Fig. 1. The water depth is $h = 0.40$ m and the maximum bottom orbital velocity is $u_m = 0.32$ m/s. The wave period is $T = 4.5$ s and thus, the wave height and wavelength are calculated to be $H = 0.12$ m and $\lambda = 8.80$ m, respectively, with KC $= u_m T/D = 14.60$. The dimensionless parameters of the wave, i.e., the relative depth $kh = 0.28(< 0.31)$, is found to be smaller than the limiting value for the shallow water wave as calculated using the linear wave theory and the wave steepness

No.	D (m)	dx (m)	L (m)	DF	Sim S/D	Exp S/D
(a) Grid convergence study in 2D NWT without a sediment bed						
$A1$	-	0.05	28.0	-	–	–
$A2$	-	0.03	28.0	-	–	–
$A3$	-	0.02	28.0	-	–	–
$A4$	-	0.01	28.0	-	–	–
(b) Grid convergence study in a reduced-length 2D NWT						
$B1$	-	0.05	4.4	-	–	–
$B2$	-	0.03	4.4	-	–	–
$B3$	-	0.02	4.4	-	–	–
$B4$	-	0.01	4.4	-	–	–
(c) Domain size optimisation, 3D NWT with sediment bed						
$C1$	0.10	0.02	28.0	6.7	0.24	0.25
$C2$	0.10	0.02	4.4	6.7	0.23	0.25
(d) Partial decoupling study						
$D1$	0.10	0.02	4.4	25	0.23	0.25
$D2$	0.10	0.02	4.4	13	0.23	0.25
$D3$	0.10	0.02	4.4	8.4	0.23	0.25
$D4$	0.10	0.02	4.4	6.7	0.23	0.25

Table 1: List of numerical tests conducted for the wave-induced scour around a single pile. The incident wave characteristics; $kh = 0.28$, $kH = 0.08$, $T = 4.5$ s, $u_m = 0.32$ m/s and KC = 14.6. The sediment bed characteristics; $d_{50} = 0.18$ mm, $\rho = 2700$ kg/m^3 and $\theta_c = 0.047$.

$kH = 0.08(< 0.9)$ is much smaller than the maximum value of wave steepness for the steep waves; clearly corresponds to the generation of the stable and the plane linear waves of low wave crest in the shallow water. The bed material consists of sand with the median particle size of $d_{50} = 0.18$ mm. The sediment density is $\rho_s = 2700$ kg/m^3 and the critical Shields parameter for the bed material is $\theta_c = 0.047$. The sediment bed is assumed to be hydraulically rough with a roughness height of $k_s = 3d_{50}$.

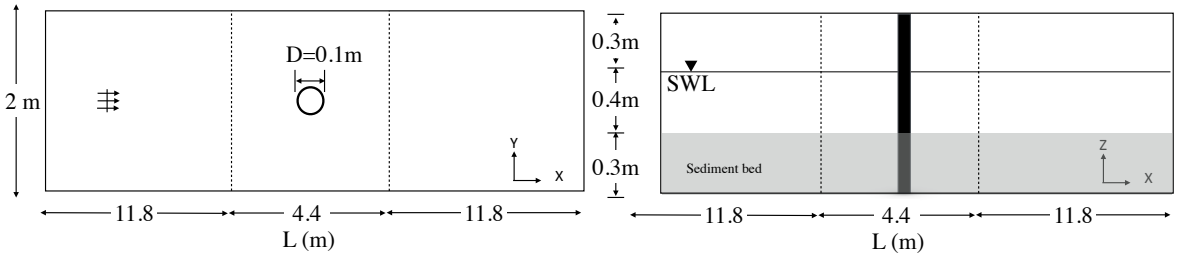

(a) Top view (b) Side view

Figure 1: Numerical setup for the validation. Length of the full-sized NWT is L= 28.0 m, width B = 2.0 m, diameter of the individual piles, D = 0.10 m. Dotted lines represent reduced-length NWT domain of L = 4.4 m. Source of the experimental data: Sumer et al. (1992).

3.1 Wave generation in a full-sized NWT

The quality of the wave generation and propagation is tested with a grid convergence study in a 2D NWT. The length of the NWT is equal to the experimental setup, i.e. L = 28.0 m as shown in Fig. 1. Waves are generated and absorbed using the relaxation and AWA method, respectively. One wave probe is located at the center of the tank where the pile is fixed. Different grid sizes of dx = 0.05 m, 0.04, 0.03 m, 0.02 m, and 0.01 m are tested. Based on the time step convergence study from the previous studies using the same model (Bihs et al., 2016; Bihs and Kamath, 2017), the Courant-Friederichs-Lewy (CFL) criterion for numerical stability is kept at a constant value of CFL = 0.2 for all tests. The tests are run for a duration of t = 60 s.

The results show the quality of the propagated wave through comparisons between the theoretical wave profile from the fifth-order cnoidal wave theory and the simulated wave elevation. Fig. 2(a) shows the wave elevation for dx = 0.05 m. The simulated wave crests and troughs are relatively lower and out of the phase compared to the theoretical data. Figs. 2(b-e) show the wave elevation for the finer grid sizes of dx = 0.04 m, 0.03 m, 0.02 m and 0.01 m. It is found that the results improve as the grid size decreases. Fig. 2(f) shows the discrepancy (δ) between the simulated wave and the wave theory. The calculation of the δ is defined in Fig. 2(f). It is seen that the discrepancy in the wave crests (δ_{cr}) decreases from 10% to 1%; the discrepancy in the wave troughs (δ_{tr}) reduces to 5% to 0.5% as dx decreases from 0.05 m to 0.01 m. The discrepancy in wave phases (δ_{ph}) is 3% for dx = 0.05 m and is reduced to 1% for dx = 0.01 m. Overall, it is seen that the simulated waves show a good agreement with the wave theory for dx = 0.02 m and 0.01 m, with almost the same accuracy of $\delta \leq 1.5\%$. Hence, the solution is considered to be converged at dx = 0.02 m.

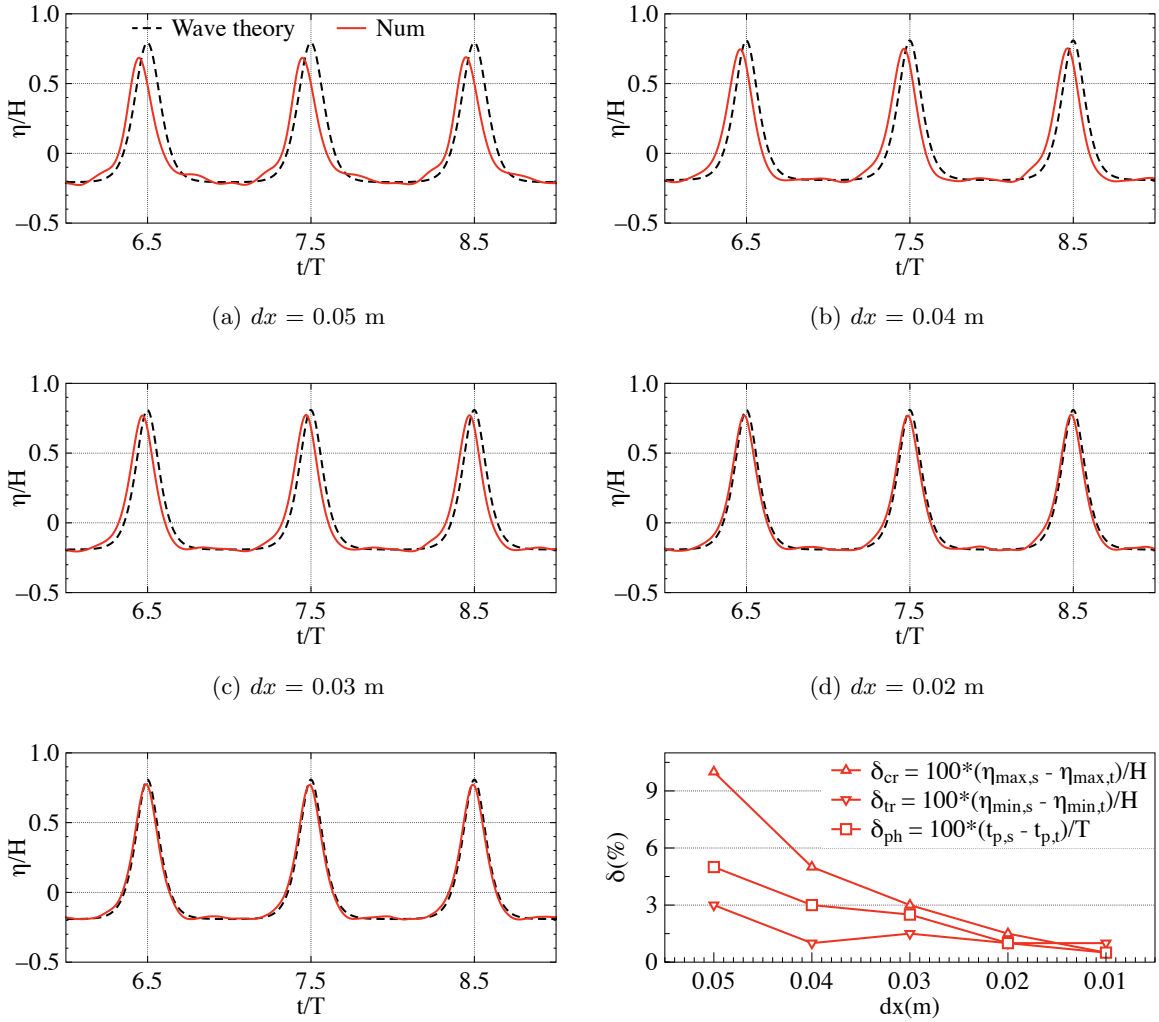

(a) dx = 0.05 m

(b) dx = 0.04 m

(c) dx = 0.03 m

(d) dx = 0.02 m

(e) dx = 0.01 m

(f) dx = 0.01 m

Figure 2: Wave generation and the grid convergence test in a full-sized NWT of L = 28.0 m. Incident wave characteristics: kh =0.28, kH =0.08, T = 4.5 s and u_m = 0.32 m/s. Wave gauge location x = 14.0 m. The red solid line shows the numerical results and the black dashed line is the wave theory. Here in Fig. 2(f); δ_{cr} is the discrepancy in wave crests, δ_{tr} is the discrepancy in wave troughs, δ_{ph} is the wave discrepancy in wave phase, $\eta_{max,s}$ is the simulated wave crest, $\eta_{max,t}$ is the theoretical wave crest, $\eta_{min,s}$ is the simulated wave trough, $\eta_{max,t}$ is the theoretical wave trough, $t_{p,s}$ is the simulated wave crest time and $t_{p,s}$ is the theoretical wave crest time.

3.2 Wave generation in a reduced-length NWT

The wave generation in a long NWT requires large computational resources. On the other hand, a similar wave can be generated and propagated in a reduced-length NWT using the AWA method. This method allows the numerical modelling of the waves propagating through the domain, which can be even shorter than one wavelength. In this study, application of the AWA method for the wave generation and propagation in a reduced-length NWT is explored. The length of the NWT is assumed to be half of the wavelength, i.e. $L = \lambda/2 = 4.4$ m. Similar to the previous grid convergence study, the grid sizes of $dx = 0.05$ m, 0.04 m, 0.03 m, 0.02 m and 0.01 m are tested. Waves are generated and absorbed using the AWA method. Tests are run for a duration of $t = 60$ s and finally the wave elevations are compared with the wave theory. Fig. 3(a) shows the wave elevation for $dx = 0.05$ m. It is found that the wave crests are marginally damped with a small phase shift. The wave troughs also show a small deviation from the theoretical values. Figs. 3(b-e) show the wave elevation for $dx =$ 0.04 m, 0.03 m, 0.02 m and 0.01 m. It can be seen that the quality of the wave improves with grid size reduction. Fig. 3(f) shows the discrepancy (δ) between the simulated wave and the wave theory. It is seen that δ_{cr} decreases from 3% to 1% as dx decreases to 0.01 m, showing good fit of the results with the wave theory as compared to full-sized NWT. However, δ_{tr} is slightly larger, decreasing from 4.5% to 1.5% as dx decreases to 0.01 m. Wave phases show good agreement with wave theory, even in the case of the coarse grid size. The maximum δ_{ph} is 1.5% for the coarse grid size and decreases to almost zero for $dx = 0.02$ and 0.01 m. Hence, the solution is considered to be converged at $dx = 0.02$ m. In addition, a similar wave propagation is seen between the reduced-length NWT and the full-size NWT, in which the simulated waves show a discrepancy of $\delta \leq 1.5\%$ for the converged grid size of $dx = 0.02$ m. This confirms the accuracy of the wave generation and the propagation in a reduced-length NWT using the AWA method.

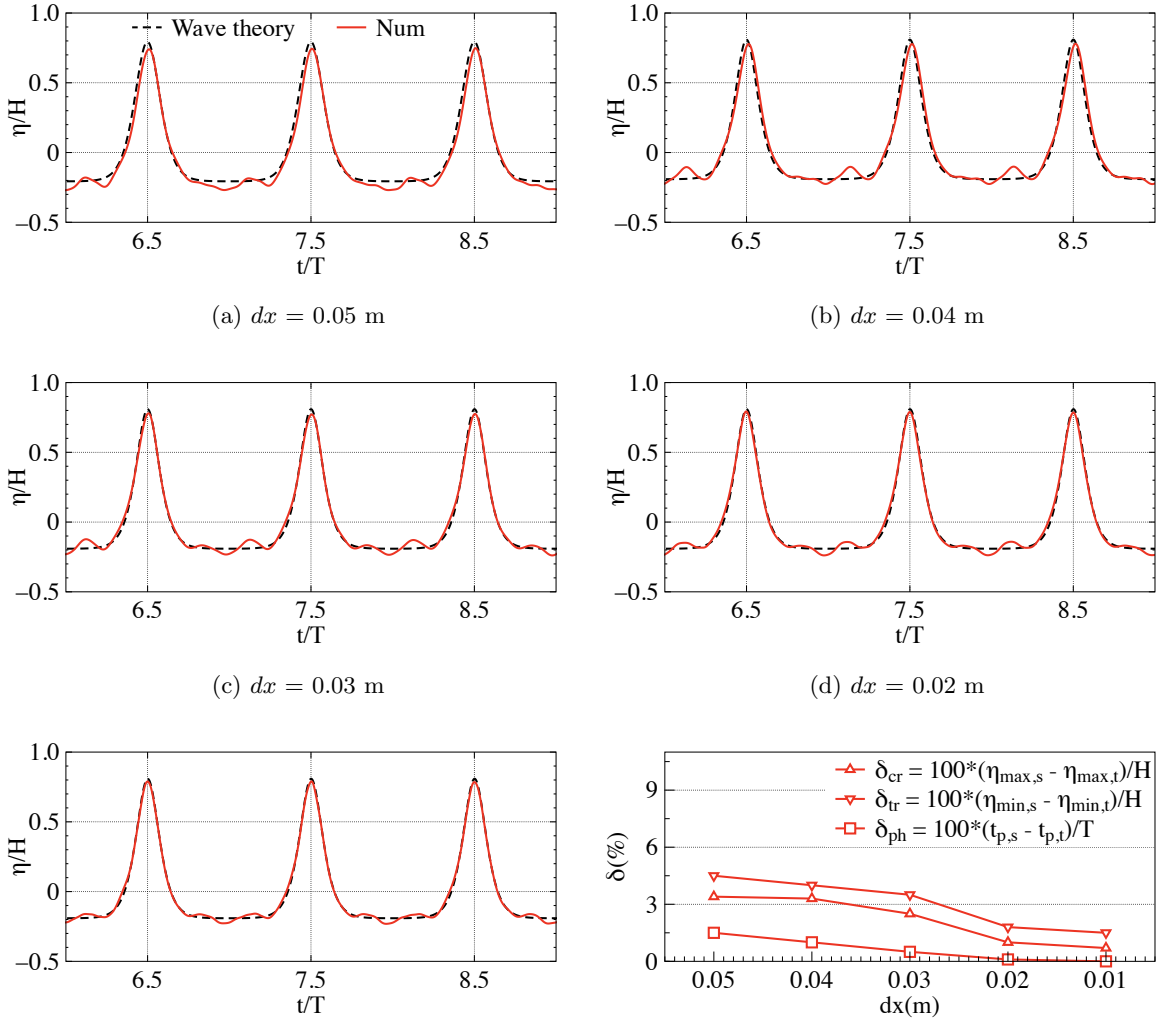

(a) $dx = 0.05$ m (b) $dx = 0.04$ m

(c) $dx = 0.03$ m (d) $dx = 0.02$ m

(e) $dx = 0.01$ m (f) $dx = 0.01$ m

Figure 3: Wave generation test in a reduced-length NWT of $L = 4.4$ m as in Fig 2.

3.3 Scour calculations in a full-sized and reduced-length 3D NWT

The simulations are carried out in a 3D NWT with the sediment bed and a pile is placed at the center of the NWT as shown in Fig. 1. The main objective of the tests is to compare the wave-induced scour calculations in a full-sized and a reduced-length NWT. The first simulation is carried out in a full-sized NWT of length $L = 28.0$ m. The width of the NWT is B = 2 m, which is assumed to be sufficiently wide to maintain an undisturbed flow around the pile (Breuer et al., 2000). The model is first run without sediment transport calculations to get fully developed waves in the NWT. The flow simulation time before sediment transport starts is $t = 25$ s and then the morphological module is turned on for scour modelling. The scouring process run time is 3600 s. Results are plotted for the equilibrium scour and the temporal

variation of the scouring process. The simulated maximum scour (S/D) in the region around the pile is presented without distinguishing between specific locations such as behind or beside the pile.

In the second test, the length of the NWT is reduced to $L = 4.4$ m. The other test conditions such as the grid size, the time step size for the morphological module, the start-up period and the total simulation run time are the same as in the first case. Finally, the results of the maximum scour depth and the temporal variation of the process are compared with the experimental data (Sumer et al., 1992).

Figs. 4(a-b) show a comparison of the scour along with free surface around a pile in a full-sized NWT of $L = 28.0$ m and a reduced-length NWT of $L = 4.4$ m. It is seen that the maximum scour takes place at the upstream side of the pile and is deposited downstream. The magnitude of the normalised maximum scour depth is $S/D = 0.23$, which matches with the experimental scour depth. Figs. 4(c-d) show the zoomed-in view of the maximum scour around the pile. It is clear from the figures that the location and pattern of the scour holes are identical. This is due to the similar quality of the waves generated in a full-sized and reduced-length NWT. Figs. 4(e-f) present a comparative view of the temporal variation of the scouring process. It can be seen that the scour depths developed with the wave crest-trough action are well captured. The wave-induced scour depth grows rapidly in the beginning and reaches the equilibrium scour state after almost half of the process run-time. The curve also shows some abrupt drops in the wave-induced scour after $t > 1500$ s. This is due to the sand-slide algorithm where the maximum scour depth is reduced when the bed slope exceeds the angle of repose (φ) and the excess sediments slump into the neighbour bed cells. The temporal variation of the scouring process is found to be in good agreement with the experimental data. However, a small difference between the simulated and the experimental scour topography can be seen. This can be attributed to the slightly over-predicted wave troughs and the use of wall functions to calculate the bed shear stress at the solid boundary. Apart from this slight disagreement, the result confirms the equivalence between the scour calculation in the reduced-length NWT and the full-sized NWT.

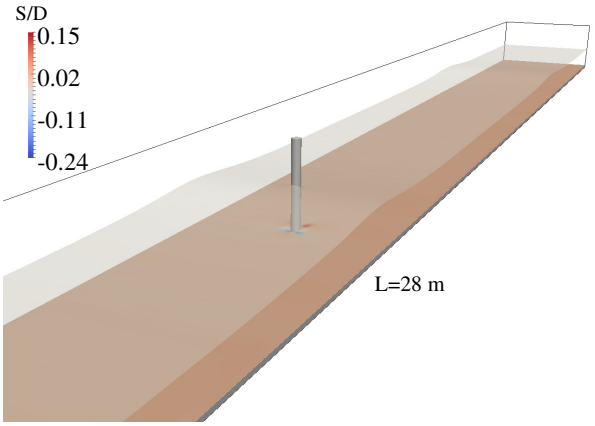

(a) Full-sized NWT, L = 28.0 m

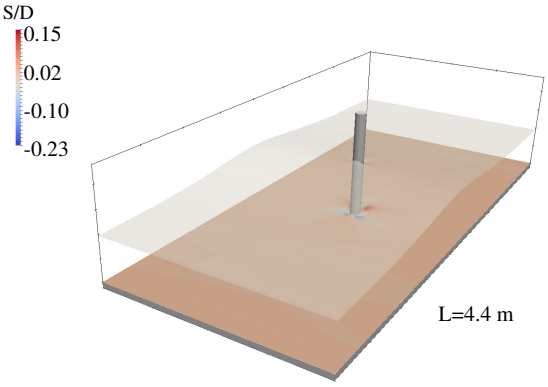

(b) Reduced-length NWT, L= 4.4 m

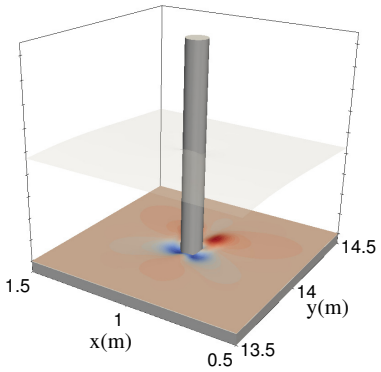

(c) Zoomed-in view of the scour for L = 28.0 m

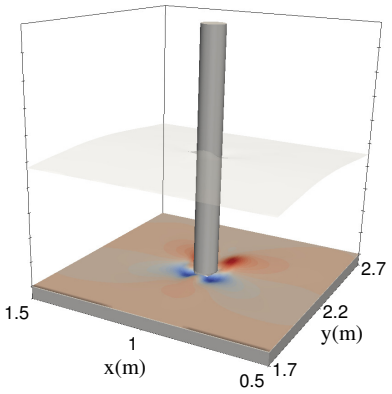

(d) Zoomed-in view of the scour for L = 4.4 m

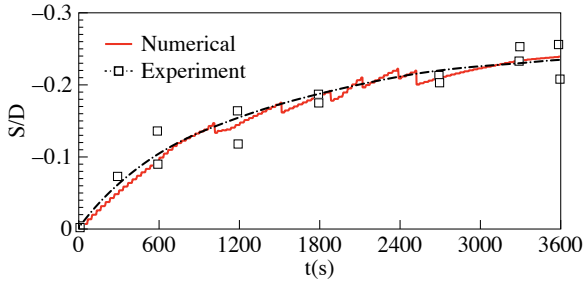

(e) Temporal variation of the scour, L = 28.0 m

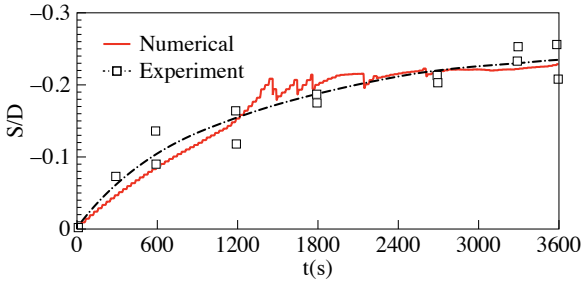

(f) Temporal variation of the scour, L = 4.4 m

Figure 4: Comparison of the simulated scour depths and the temporal variation of the scouring process in a full-sized NWT of L = 28.0 m (on the left) and a reduced-length NWT of L = 4.4 m (on the right). The red solid line shows the numerical result and the black squares with the black dotted line show the experimental scour depth around the pile (Sumer et al., 1992).

3.4 Partial decoupling

In a real case scenario, the time scales associated with the flow are much smaller than that of the morphological evolution. Hence, when the sediment bed morphology is evolving, it takes place so slowly that the small morphological changes do not affect the flow hydrodynamics significantly. This concept allows the partial temporal decoupling of the time scales of the morphological and hydrodynamic models. Here, the decoupling means a larger time step for the sediment transport calculations compared to the time step for the flow, i.e. DF = $\Delta t_s/\Delta t$, where Δt_s is the time step for the morphological model, Δt is the time step for the hydrodynamic model and DF is the decoupling factor. This implies that a time step larger than the hydrodynamic time step can be used for the scour calculations, instead of solving the scouring process as a fully coupled model which demands large computation resources (Nelson et al., 2005).

In this subsection, the partial temporal decoupling of the time scales for the morphological and hydrodynamic models with the decoupling factors DF = 25, 12.5, 8.8 and 6.6 is investigated. The flow simulation time between the transport calculation is $\Delta t/T = 1/150$. The time step for the sediment transport is calculated to be Δt_s = DF x Δt. Thus, the morphological run for a duration of t = 3600 s is achieved by imposing N = 30, 60, 90 and 120 number of waves with DF = 25, 12.5, 8.8 and 6.6, respectively.

Fig. 5(a) shows the temporal variation of the scouring process by imposing N = 30 waves with DF = 25. The fluctuations in the curve represent the instantaneous increase in the scour depth during the wave crest action and is referred to as local wave scour peaks. The local scour pattern seems to be progressive in a staircase pattern. This means the major scour takes place during the wave crest action while moving towards the equilibrium scour. Fig. 5(b) shows the temporal variation of the scouring process by imposing N = 60 waves with DF = 12.5. It can be seen that the number of the local wave scour peaks in the curve increases with a decreasing DF, as the number of waves increases. However, the equilibrium scour depth and the temporal variation of the scouring process is the same. Figs. 5(c-d) show the results of the scouring process achieved by imposing N = 90 and 120 waves with DF = 8.8 and 6.6, respectively. As expected, an increase in number of waves with lower DF values further increases the number of local wave scour peaks developed with the wave action. However, the equilibrium scour depth is the same. The results of the scouring process by increasing the number of waves and decreasing the DF values are in agreement with the experimental data. Hence, it appears that although a further reduction in the decoupling factor DF captures more local wave scour peaks generated with the wave action, the equilibrium scour depth and the temporal variation of the scour are the same. The results confirm the applicability of the partial decoupling approach. The implication of these results is that the simulations can be carried out by imposing N = 120 waves with DF = 6.6, so that the maximum scour can be simulated with an optimal flow simulation time.

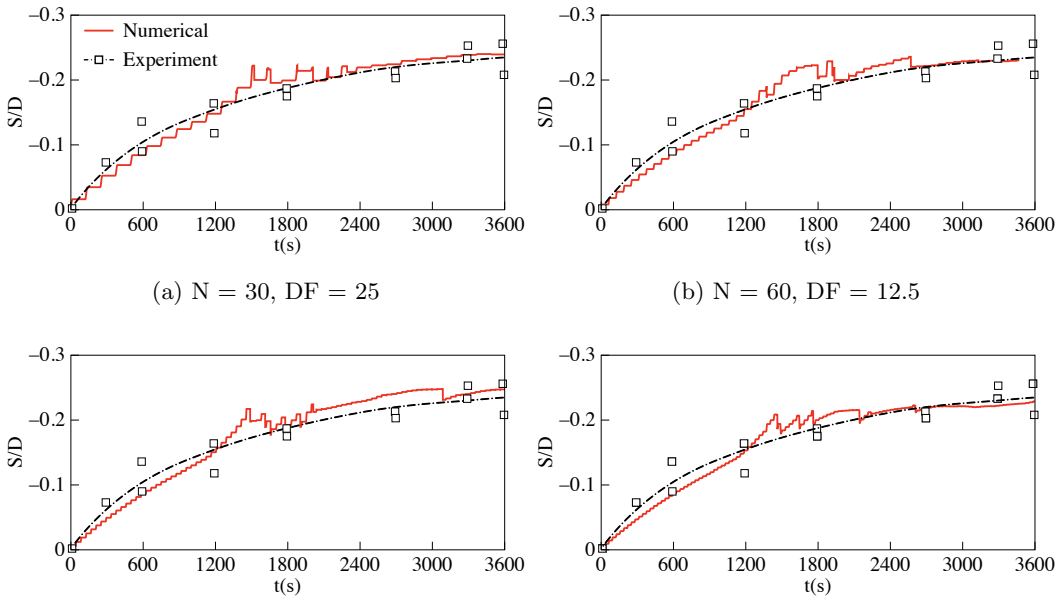

(a) N = 30, DF = 25

(b) N = 60, DF = 12.5

(c) N = 90, DF = 8.8

(d) N = 120, DF = 6.6

Figure 5: Computed temporal variation of the scouring process for different case scenarios. Here; N is the number of incident waves and DF is the decoupling factor. The red solid line shows the numerical result and the The black squares with the black dotted line are the experimental data (Sumer et al., 1992).

4 Scour around piles in a side-by-side arrangement

The validated model is used to simulate the scour process around piles in a side-by-side arrangement. The focus is on the change in wave hydrodynamics and the resulting scour in the gap between the two piles for given values of G/D and KC. The simulations are carried out in the reduced-length NWT of $L = 4.4$ m. The numerical setup follows the experimental setup used by Sumer and Fredsøe (1998) shown in Fig. 6. The pile diameter is $D = 0.09$ m. The water depth is $h = 0.4$ m and the maximum bottom orbital velocity is $u_m = 0.26$ m/s. The wave period is $T = 4.5$ s. The wave height and the wavelength are calculated to be $H = 0.10$ m and $\lambda = 8.8$ m, respectively, resulting in KC = 13. The bottom of the NWT ($z =$ -0.3 m) is filled with sand of the median grain size $d_{50} = 0.2$ mm and the sediment density is $\rho_s = 2700\ kg/m^3$. The details of the test cases and conditions are listed in Table 2.

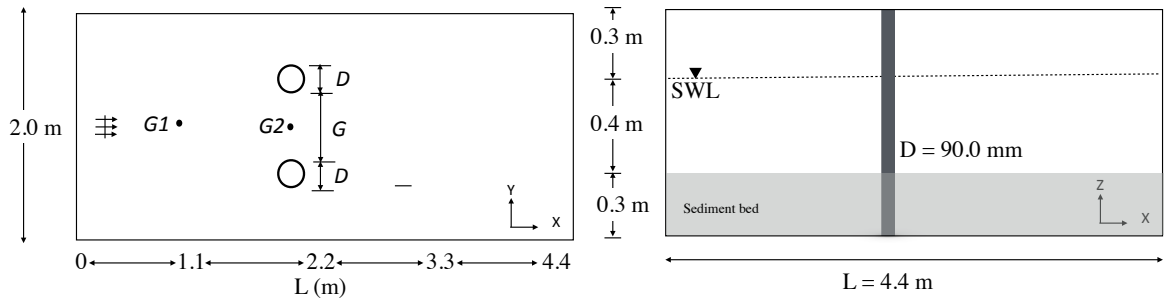

(a) Top view (b) Side view

Figure 6: Numerical setup for the piles in a side-by-side arrangement. Length of the reduced-length NWT is L= 4.4 m, width B = 2.0 m, Diameter of the individual piles, D = 0.09 m. Gauge locations (m), G1 = 1.1, 1, 0.10; G2 = 2.2, 1, 0.10. Source of the experimental data: Sumer and Fredsøe (1998)

No.	T(s)	u_m (m/s)	kh	kH	θ	KC	Q (m^3/s)	G/D	L (m)	Sim S/D	Exp S/D
(a) Variation of S/D with G/D											
$E1$	4.5	0.26	0.28	0.07	0.09	13	0	0	4.4	0.40	0.33
$E2$	4.5	0.26	0.28	0.07	0.09	13	0	0.3	4.4	0.80	0.78
$E3$	4.5	0.26	0.28	0.07	0.09	13	0	1.0	4.4	0.38	0.41
$E4$	4.5	0.26	0.28	0.07	0.09	13	0	2.0	4.4	0.25	0.28
$E5$	4.5	0.26	0.28	0.07	0.09	13	0	3.0	4.4	0.25	-
$E6$	4.5	0.26	0.28	0.07	0.09	13	0	5.0	4.4	0.23	-
(b) Variation of S/D with KC											
$F1$	1.8	0.15	0.76	0.12	0.05	3	0	0.4	4.4	0.08	0.11
$F2$	3.0	0.19	0.42	0.08	0.06	6.3	0	0.4	4.4	0.60	0.67
$F3$	4.5	0.37	0.27	0.10	0.18	19	0	0.4	4.4	0.90	0.94
$F4$	-	0.31	-	-	0.06	∞	0.25	0.4	4.4	1.30	1.50

Table 2: List of the numerical tests carried for the scour around the piles in a side-by-side arrangement. The sediment bed characteristics; d_{50} = 0.2 mm, ρ = 2700 kg/m^3, $\varphi = 35^\circ$ and θ_c = 0.047. Experimental data source: Sumer and Fredsøe (1998)

4.1 Effect of gap ratio G/D

The main flow feature in the gap between two piles in a side-by-side arrangement exposed to waves is the increased gap flow, called the jet effect (Sumer and Fredsøe, 1998). The intensity of the jet effect depends on G/D and KC. In this subsection, the development of the jet effect for increasing G/D is investigated by analysing the wave-induced velocities in the gap when the wave-front hits the piles at $t/T = 9.25$. The KC number is KC = 13 for all numerical tests.

Fig. 7 shows the simulated free surface along with a zoomed-in XY-plane view of the wave-induced higher velocity between two piles for $G/D = 0$, 0.3, 1, 2, 3 and 5. Figs. 7(a-b) show the free surface flow around the piles for $G/D = 0$. There is no flow passing through the gap and the piles act as a single obstacle. The free surface velocity magnitude at the sides of the piles is $u = 0.53$ m/s, and the downstream side of the piles appears to be dominated by a low-velocity regime. Figs. 7(c-d) show the free surface flow and velocity in the gap between two piles when the wave front hits the piles with $G/D = 0.3$. The velocity in the gap between the two piles is increased to $u = 0.6$ m/s, while the velocity at the outer sides of the piles are almost the same as seen for $G/D = 0$. This indicates the development of the jet effect as the flow passes through the gap. Figs. 7(e-h) show the free surface flow around the piles for $G/D = 1$ and 2. For these values of G/D, the higher velocity are still seen in the gap but the magnitude reduces to $u = 0.5$ m/s; i.e. a reduction in the jet effect with a further increase in G/D. Figs. 7(i-l) demonstrate the flow around the piles for $G/D = 3$ and 5, showing that the velocities are $u = 0.45$ m/s around the individual piles and no amplified velocities in between the piles are seen. This implies that for $G/D > 2$, piles act as individual piles and do not contribute to the jet effect.

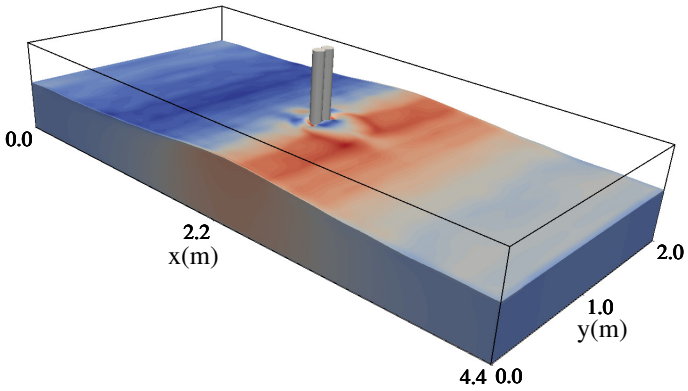

(a) 3D view, $G/D = 0$

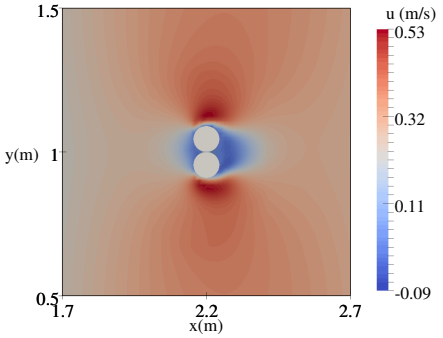

(b) XY-plan at z = 0.10 m, $G/D = 0$

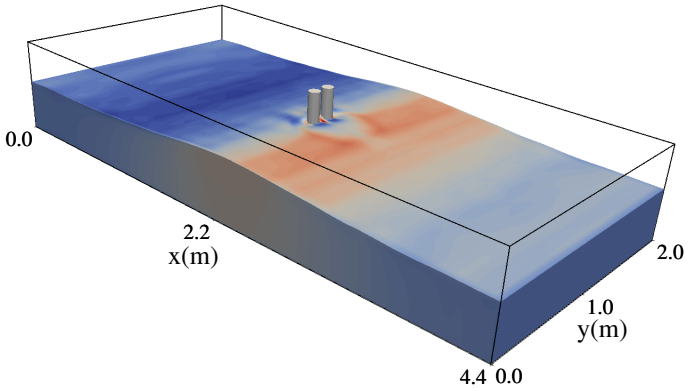

(c) 3D view, $G/D = 0.3$

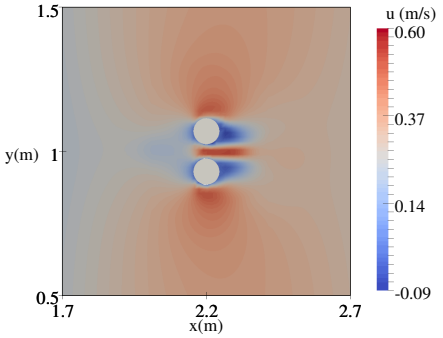

(d) XY-plan at z = 0.10 m, $G/D = 0.3$

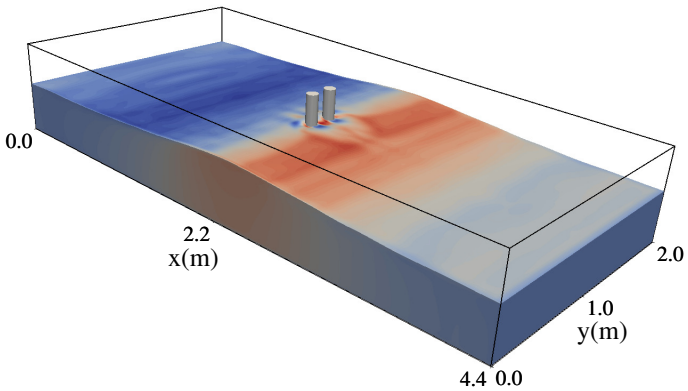

(e) 3D view, $G/D = 1$

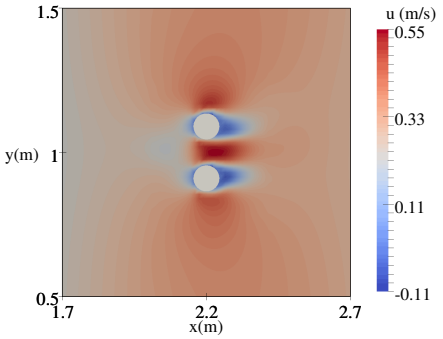

(f) XY-plan at z = 0.10 m, $G/D = 1$

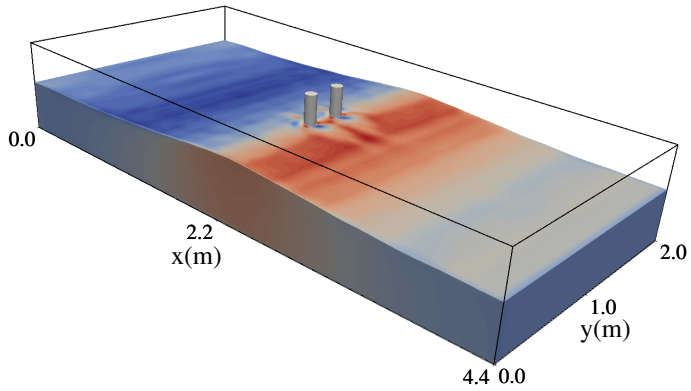

(g) $G/D = 2$

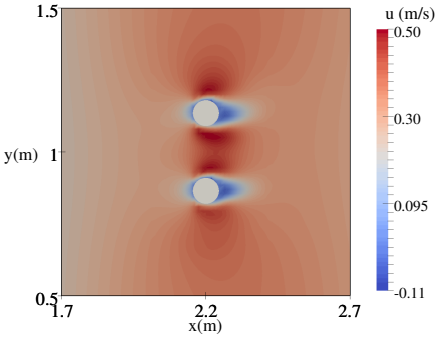

(h) XY-plan at z = 0.10 m, $G/D = 2$

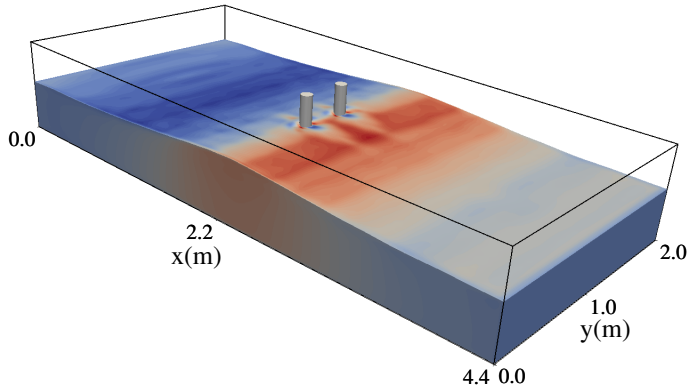

(i) $G/D = 3$

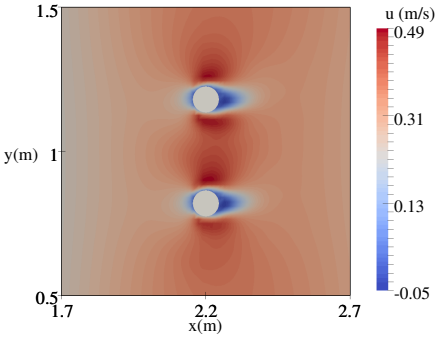

(j) XY-plan at z = 0.10 m, $G/D = 3$

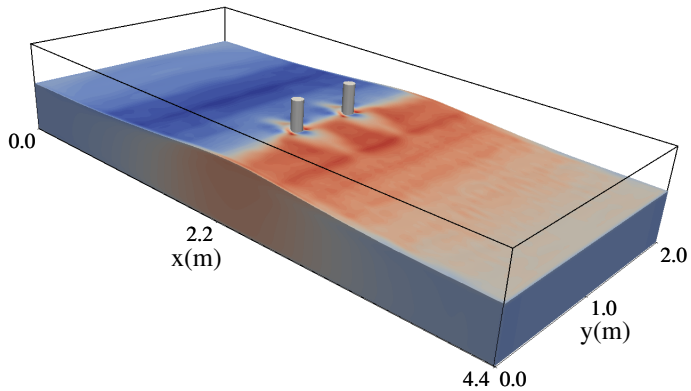

(k) $G/D = 5$

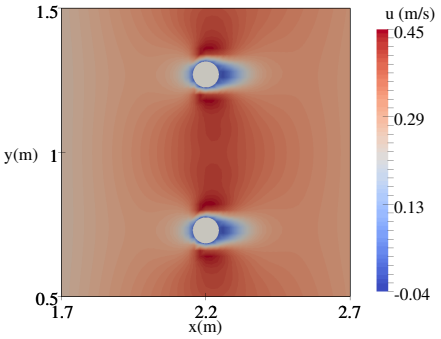

(l) XY-plan at z = 0.10 m, $G/D = 5$

Figure 7: The free surface velocities around the piles for given value of G/D when the wave front attacks the piles at $t/T = 9.25$. The incident wave characteristics; $T = 4.5$ s, $u_m = 0.26$ m/s, $D = 0.09$ m and KC = 13. The XY-plane is the zoomed-in view close to the piles to show the formation of jet effect.

Fig. 8 and Fig. 9 further elaborate on the development of the jet effect as G/D increases, by comparing the flow velocities at two different gauges. As shown in Fig. 6, a gauge $G1$ is fixed at the upstream side of the piles ($x = 1.1$ m, $y = 1$ m, $z = 0.10$ m) to capture the undisturbed flow velocities; another gauge $G2$ is placed between the two piles ($x = 2.2$ m, $y = 1$ m, $z = 0.10$ m) to capture the amplified flow velocities. The flow velocities are compared in order to quantify the relative change in the flow when the waves hit the piles. The relative change in the horizontal velocity is defined as $u_r = u_{m2}/u_{m1}$ and for the vertical velocity it is $w_r = w_{m2}/w_{m1}$. Here u_{m1}, w_{m1}, u_{m2} and w_{m2} are the peak horizontal and the peak vertical velocity at the gauges G1 and G2, respectively. Figs. 8(a-f) compare sequences of the horizontal velocity at the gauges G1 and G2; and Fig. 8(g) shows the relative change in the horizontal velocities verses G/D. It is seen that for $G/D = 0.3$, the horizontal velocities at gauge G2 are almost twice compared to the velocities at gauge G1. For $G/D = 1$ and 2, an increase in G/D results in a decrease in the relative change in horizontal velocity to $u_r = 1$. For $G/D = 3$ and 5, no change in the relative horizontal velocities are seen with a constant value of $u_r = 1$.

Figs. 9(a-g) show sequences of the vertical velocity and the relative change in the vertical velocities w_r as G/D increases. The behaviour of w_r is opposite to that of the relative change in the horizontal velocity u_r. The relative change in vertical velocity reduces to $w_r = 0.85$ for $G/D = 0.3$ and 2, and to $w_r = 0.75$ for $G/D = 1$ and approaches to $w_r = 1$ for $G/D = 3$. There is no change in w_r observed for $G/D > 3.0$. Thus, a simultaneous increase in u_r and a decrease in w_r indicate an increasing jet effect.

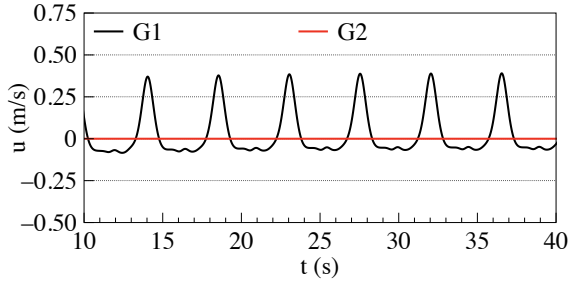

(a) G/D = 0

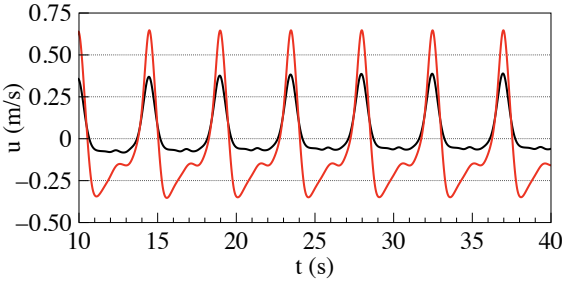

(b) G/D = 0.3

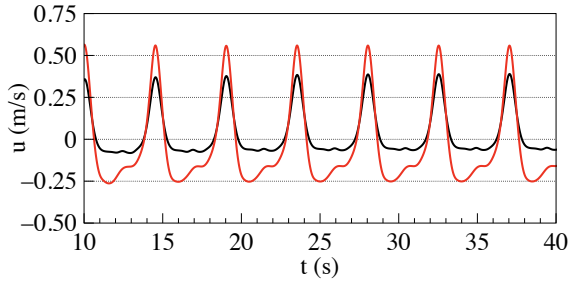

(c) G/D = 1

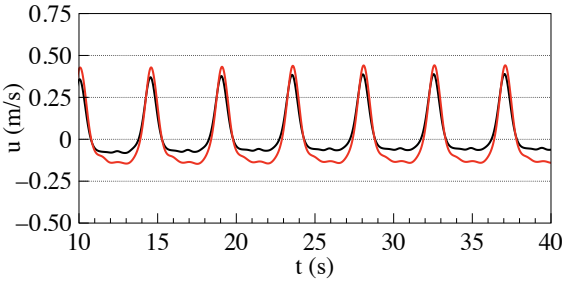

(d) G/D = 2

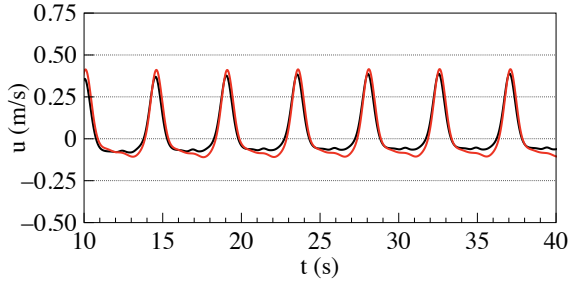

(e) G/D = 3

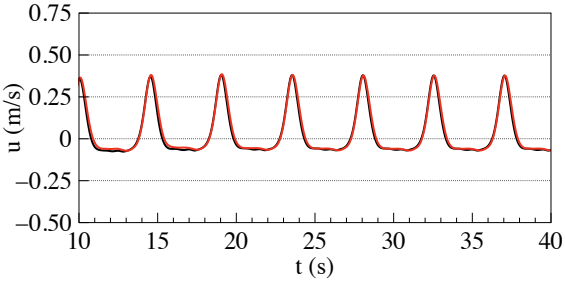

(f) G/D = 5

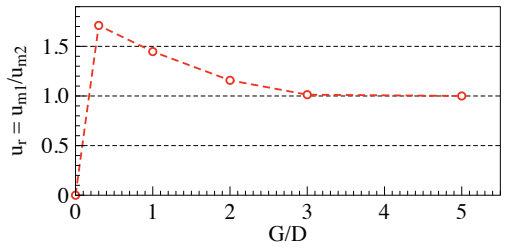

(g) u_r plotted against an increasing G/D

Figure 8: Computed relative change in the horizontal velocities verses t for given values of G/D. The incident wave characteristics; $T = 4.5$ s, $u_m = 0.26$ m/s, $D = 0.09$ m and KC = 13. (a) - (f): The black solid line shows the temporal change in u at gauge G1 = (1.1, 1, 0.10) m; the red solid line is temporal change in u at the gauge G2 = (2.2, 1, 0.10) m (see Fig. 6). (g): The red dotted line show relative change in u.

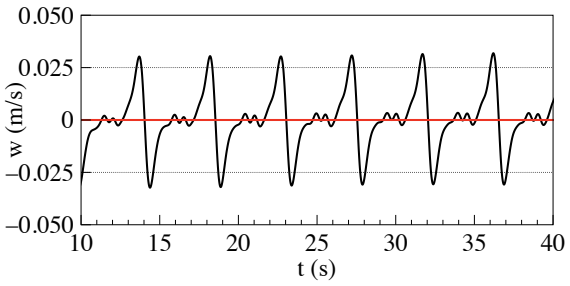

(a) G/D = 0

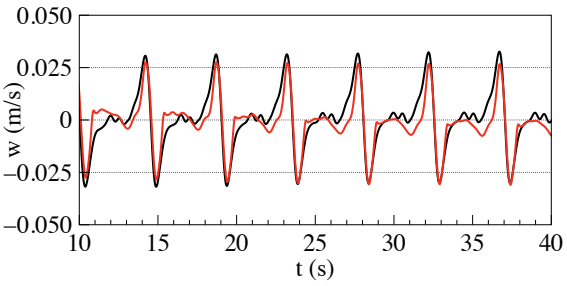

(b) G/D = 0.3

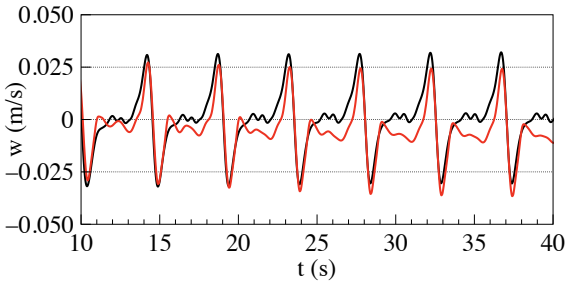

(c) G/D = 1

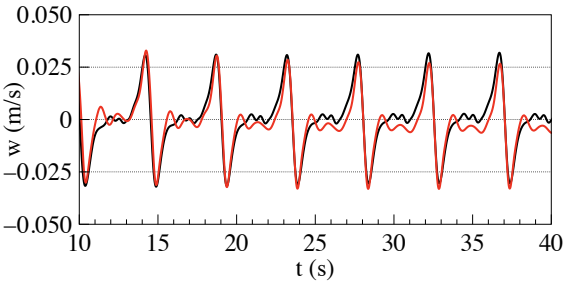

(d) G/D = 2

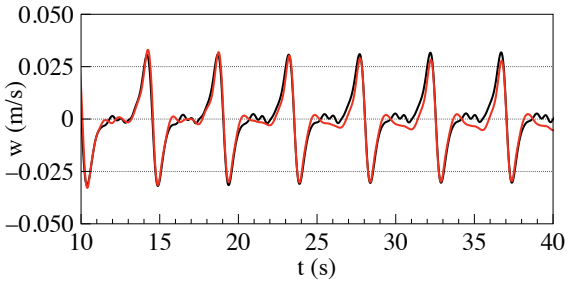

(e) G/D = 3

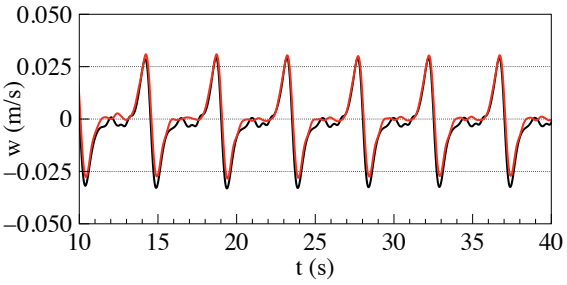

(f) G/D = 5

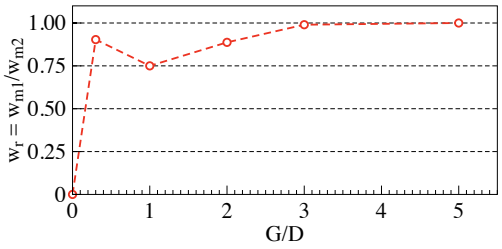

(g) w_r plotted against an increasing G/D

Figure 9: Computed relative change in the vertical velocities verses t for given values of G/D as for Fig. 8

Fig. 10 shows the 3D view of the scour around the two piles as G/D increases and a ZX-plan view of the scour with the free surface profile in the middle of the gap. The simulations are run for a duration of $t = 3600$ s. Figs. 10(a-b) show the wave-induced scour for $G/D = 0$. The normalised maximum scour depth is $S/D = 0.4$ which takes place at the outer edges of the two piles. The magnitude of the maximum scour and the deposition are almost the same. This is due to the large velocities at the side of the piles which leads to the pick up of sediments from the upstream side and is transported in the low-velocity regime downstream of the piles. Figs. 10(c-d) show the simulated scour domain for $G/D = 0.3$. The maximum scour takes place in the gap between the two piles. The major part of the eroded sediment is deposited downstream of the gap and forms a non-uniform scour hole. The magnitude of the normalised maximum scour depth is $S/D = 0.8$ which agrees with the experimental data (Sumer and Fredsøe, 1998). Figs. 10(e-h) show the scour for $G/D = 1$ and 2. It is seen that the scour area between the two piles seems to move towards the individual piles for increasing G/D. The normalised maximum scour depth is $S/D = 0.38$ and 0.25 for $G/D = 1$ and 2, respectively. The decrease in scour depth from $S/D = 0.8$ to 0.25 as G/D increases from $G/D = 0.3$ to 2 is a result of reduced jet effect as G/D increases, and consequently a reduction in the scour depth between two piles. Figs. 10(i-l) show the wave-induced scour for $G/D = 3$ and 5. For these range of G/D values, the maximum scour takes place in the proximity of the individual piles and no erosion takes place in the gap, as shown in the ZX-plane view of the scour. The numerical findings agree with the study carried out by Sumer and Fredsøe (1998), which suggests that for $G/D > 2$ piles in a side-by-side arrangement each acts as an individual pile and depicts two very distinct scour holes.

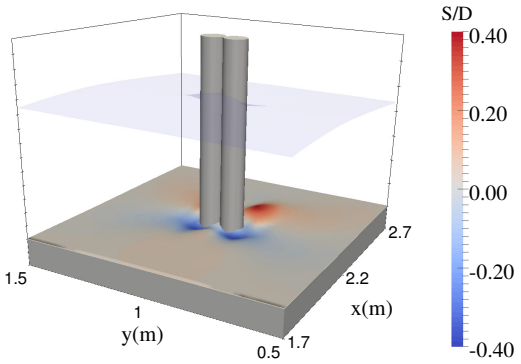

(a) 3D view, $G/D = 0$

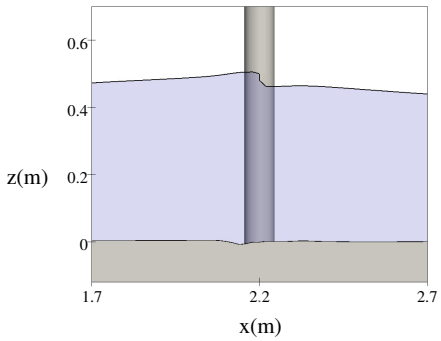

(b) ZX-plane at y = 1 m, $G/D = 0$

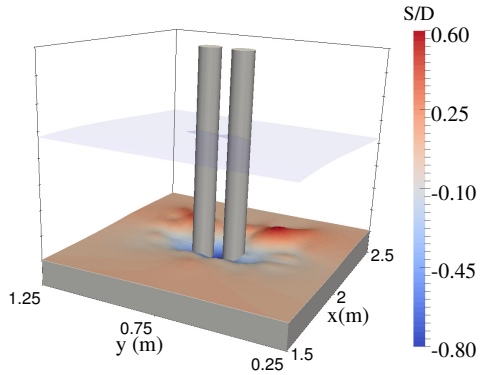

(c) 3D view, $G/D = 0.3$

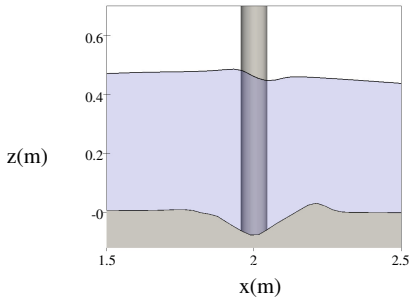

(d) ZX-plane at y = 0.75 m, $G/D = 0.3$

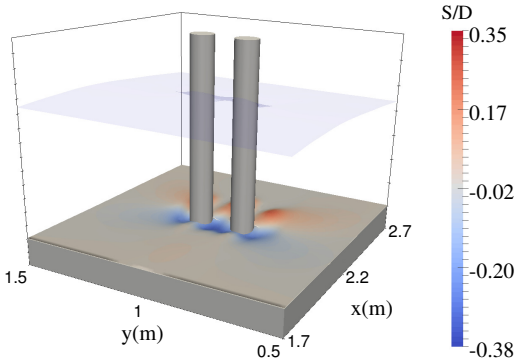

(e) 3D view, $G/D = 1$

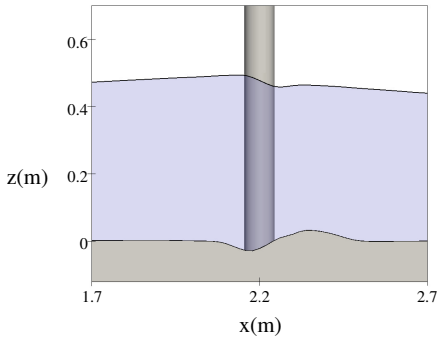

(f) ZX-plane at y = 1 m, $G/D = 1$

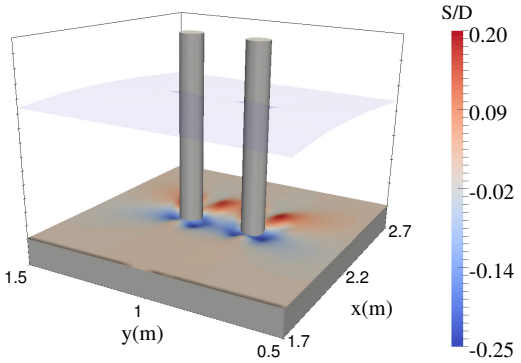

(g) 3D view, $G/D = 2$

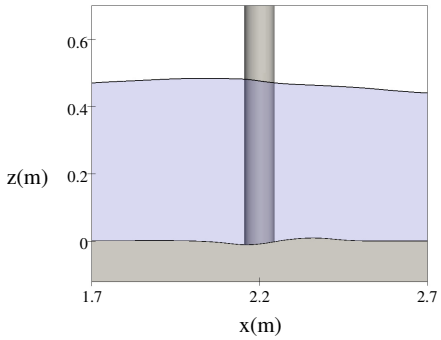

(h) ZX-plane at y = 1 m, $G/D = 2$

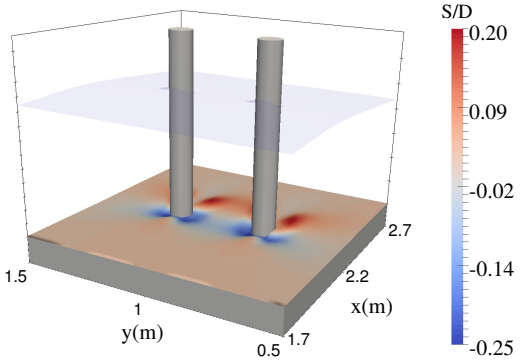

(i) 3D view, $G/D = 3$

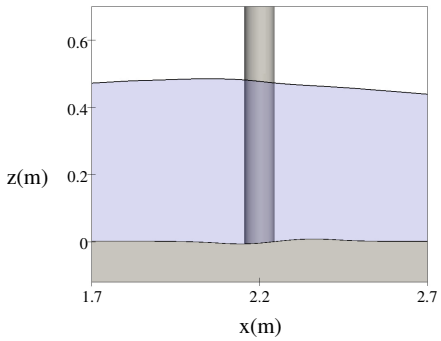

(j) ZX-plane at y = 1 m, $G/D = 3$

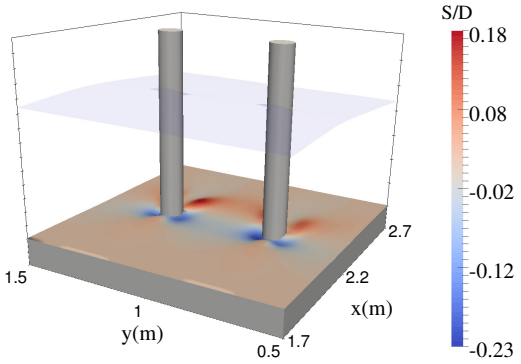

(k) 3D view, $G/D = 5$

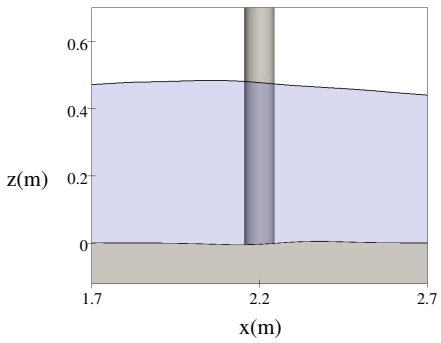

(l) ZX-plane at y = 1 m, $G/D = 5$

Figure 10: The simulated scour with free surface profile for given values of G/D. The incident wave characteristics; $T = 4.5$ s, $u_m = 0.26$ m/s, $D = 0.09$ m and KC = 13.

Fig. 11 presents the comparison between simulated and experimental scour hole extents. The parameter l_x and l_y are the lengths of the scour affected domain in $x-$ and y-directions, respectively. Fig. 11(a) shows the variation of the normalised scour extent l_x/D as G/D increases. It appears that the variation of the scour extent in the x-direction is almost similar to the change in the jet effect as G/D increases. The scour extent in the $x-$direction is maximum for $G/D = 0.3$, then it starts decreasing to $l_x/D = 2$ as $G/D =$ increases from 2 to 3, reaching a nearly constant value of $l_x/D = 2$ for $G/D > 2$. Fig. 11(b) shows the variation in the normalised scour extent l_y/D in the y-direction. It appears that l_x/D increases as G/D increases up to $G/D = 2.0$, reaching a almost constant value for $G/D > 2$. Eventually, no change in l_x/D and l_y/D for $G/D > 2$ indicates two distinct scour holes around the individual piles.

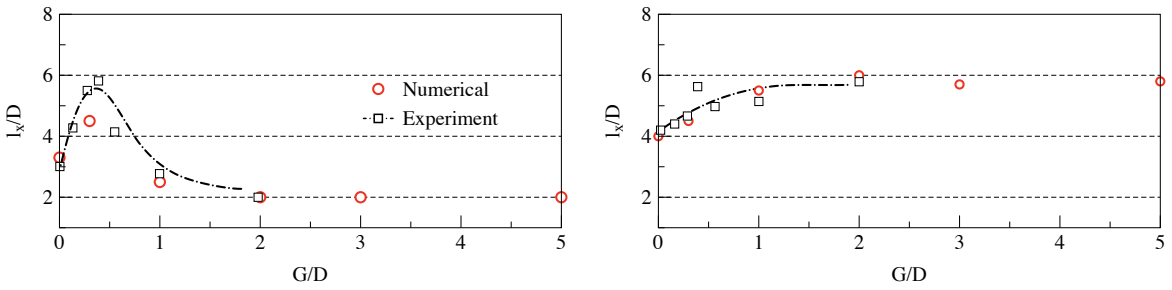

(a) The normalised scour extent in x-direction

(b) The normalised scour extent in y-direction

Figure 11: Change in the scour extent in x and y-direction as G/D increases. The red circles show the numerical results and the black squares with the dotted line are the experimental result (Sumer and Fredsøe, 1998).

Figs. 12(a-f) present the temporal variation of the scouring process plotted for $G/D = 0.0, 0.3, 1, 2, 3, 5$, respectively. The simulations are run for $t = 3600$ s. It is found that the major part of the maximum scour takes place within the first $t = 1000$ s of the scouring process and then the curve starts approaching the equilibrium scour state. The fluctuations in the scour depth pattern, i.e. the local wave scour peaks, represents the scouring and refilling with the wave crest-trough action. Results demonstrate that the magnitude of the local wave scour peaks seems to change with G/D which is due to the jet effect between the two piles.This can be seen for $G/D = 0.3$ that the local wave scour peaks are higher compared to other G/D values which is attributed to the largest jet effect for $G/D = 0.3$.

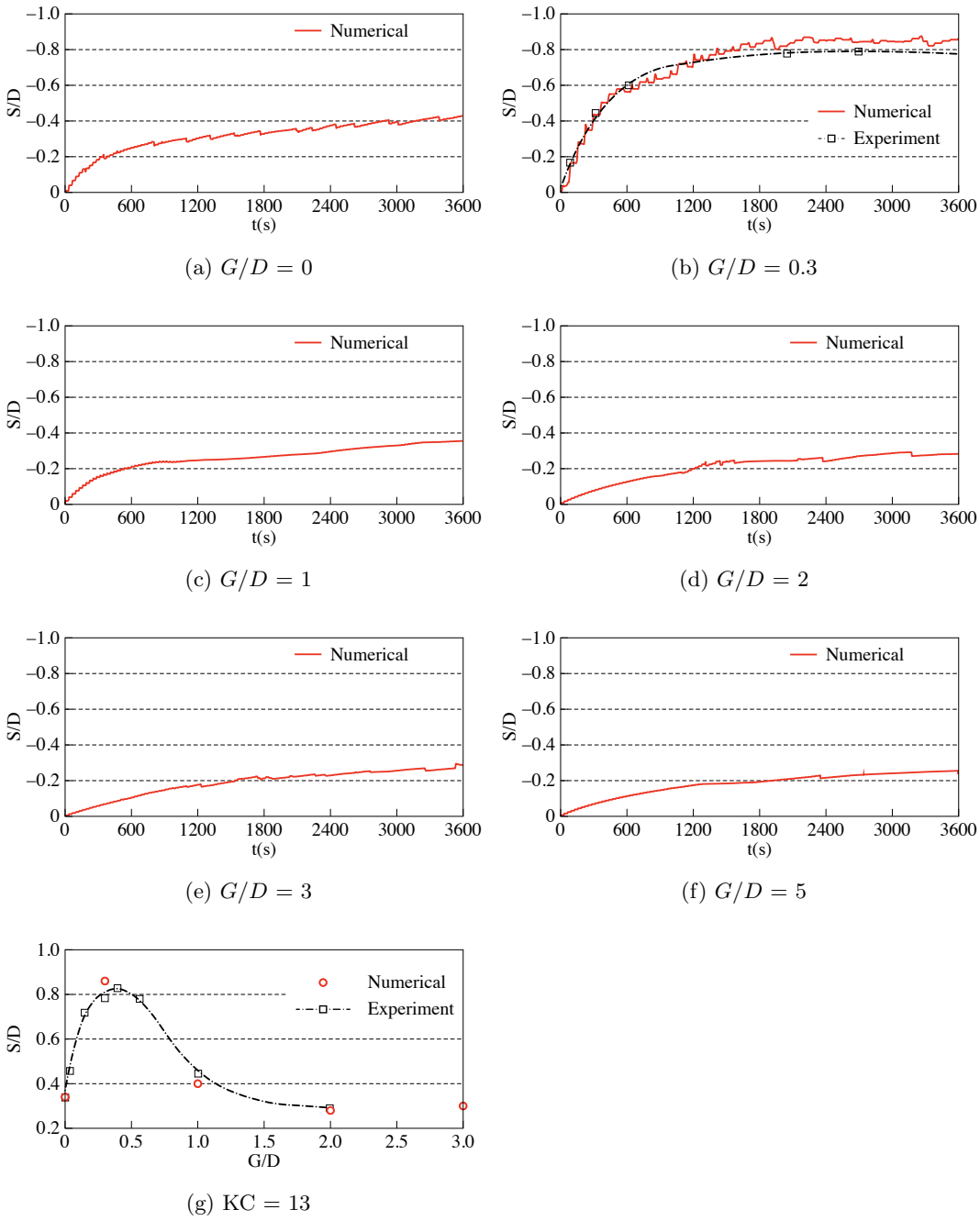

(a) $G/D = 0$ (b) $G/D = 0.3$

(c) $G/D = 1$ (d) $G/D = 2$

(e) $G/D = 3$ (f) $G/D = 5$

(g) KC = 13

Figure 12: Temporal variation of the wave-induced scour and the variation in the normalised maximum scour depth S/D for given values of G/D, KC =13. The red solid line shows the simulated temporal variation of wave-induced scour, the red circles are the normalised maximum scour depth and the black squares with the dotted line are the experimental result (Sumer and Fredsøe, 1998).

Fig. 12(g) shows and compares the variation of the normalised maximum scour depth

S/D as G/D increases. It is found that the maximum scour depth increases from $S/D = 0.4$ to 0.8 for $G/D = 0$ to 0.3 and decreases then to $S/D = 0.25$ for the G/D range $0.3 \leq G/D \leq 2$. Further increase in the gap ratio ($G/D > 2$) leads to no change in S/D. Finally, the result for the change in S/D as G/D increases, is in good agreement with the experimental data (Sumer and Fredsøe, 1998).

4.2 Effect of KC number

In this subsection, the effect of the KC number on the wave-induced scour is discussed. The gap ratio is $G/D = 0.4$ for all simulations. Figs. 13(a-b) shows the scour contour for KC = 3. In this case, the maximum bottom orbital velocity is $u_m = 0.15$ m/s and the far field Shields parameter, $\theta = 0.05$, where the critical Shields parameter is, $\theta_c = 0.047$. Here, the wave-induced scour occurs in the clear water scour regime. Thus, when such a relatively small wave hits the piles, the wave impact contributes to a low bed shear stress around the piles that can only initiate weak sediment particle movement. On the other hand, relatively large velocities in the gap between two piles compared to the velocities throughout the domain are the main reason for the sediment transport for a low KC number. In this case, the normalised maximum scour depth in the gap is found to be $S/D = 0.08$. Figs. 13(c-f) show the maximum scour for KC = 6.3 and 19. The maximum bottom orbital velocity $u_m = 0.2$ m/s for KC = 6.3, $u_m = 0.37$ m/s for KC = 19 and the corresponding far field Shields parameters are, $\theta = 0.06$ and 0.18, respectively. As the far field Shields parameter is greater than the critical Shield parameter, clearly indicating the wave-induced scour in the live-bed regime. The presence of piles give high velocity around the piles and relatively larger velocity in the gap, consequently more sediment transport around the piles and the maximum scour depth in the gap between the two piles. The normalised maximum scour depth is found to be, $S/D = 0.6$ for KC = 6.3 and $S/D = 0.9$ for KC = 19.

Figs. 13(g-h) show the scour for KC = ∞. Here, scour occurs under a steady current of mean velocity, $u = 0.31$ m/s, and the far field Shields parameter, $\theta = 0.06$. The scour around the piles takes place in a relatively moderate live-bed scour regime compared to the wave-induced scour for KC=19. In addition, the scour due to the reverse flow is observed to be negligible for steady flow, unlike for the scour under waves. Thus, a unidirectional steady flow impacting the piles leads to an increase in the velocity around the piles and the formation of the unidirectional jet in the gap, resulting in a deep scour hole of magnitude $S/D = 1.3$.

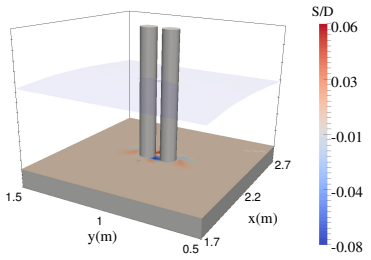

(a) 3D view, KC = 3

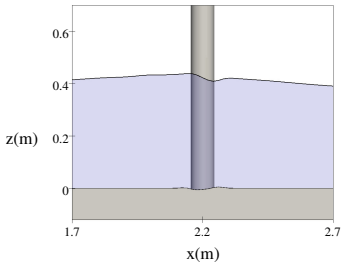

(b) ZX-plane at y = 1 m, KC = 3

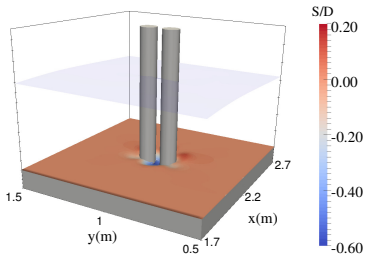

(c) 3D view, KC = 6.3

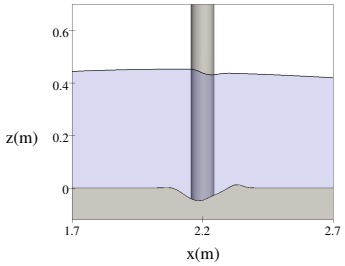

(d) ZX-plane at y = 1 m, KC = 6.3

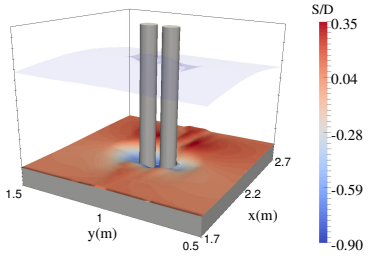

(e) 3D view, KC = 19

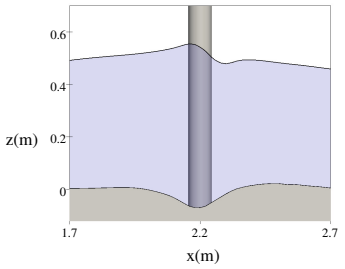

(f) ZX-plane at y = 1 m, KC = 19

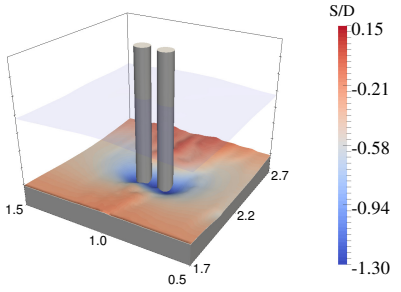

(g) 3D view, KC = ∞

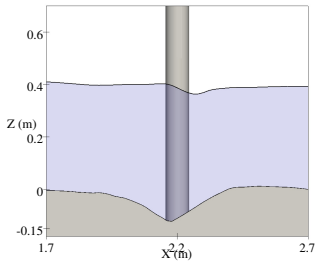

(h) ZX-plane at y = 1 m

Figure 13: The simulated scour with free surface profile for given values of KC, $G/D = 0.4$

Figs. 14 (a-d) show the temporal variation of the wave-induced scour for KC = 3, 6.3, 19, ∞, respectively. The jet effect in the gap between the piles is the prime factor causing the maximum scour. It is seen that the temporal variation of the wave-induced scour is similar for all values of KC. It grows rapidly in the beginning and then slows down as it approaches equilibrium. This is due to the fact that the bed shear stress decreases with scour hole development (Roulund et al., 2005) and results in attenuation of the scour rate over time.

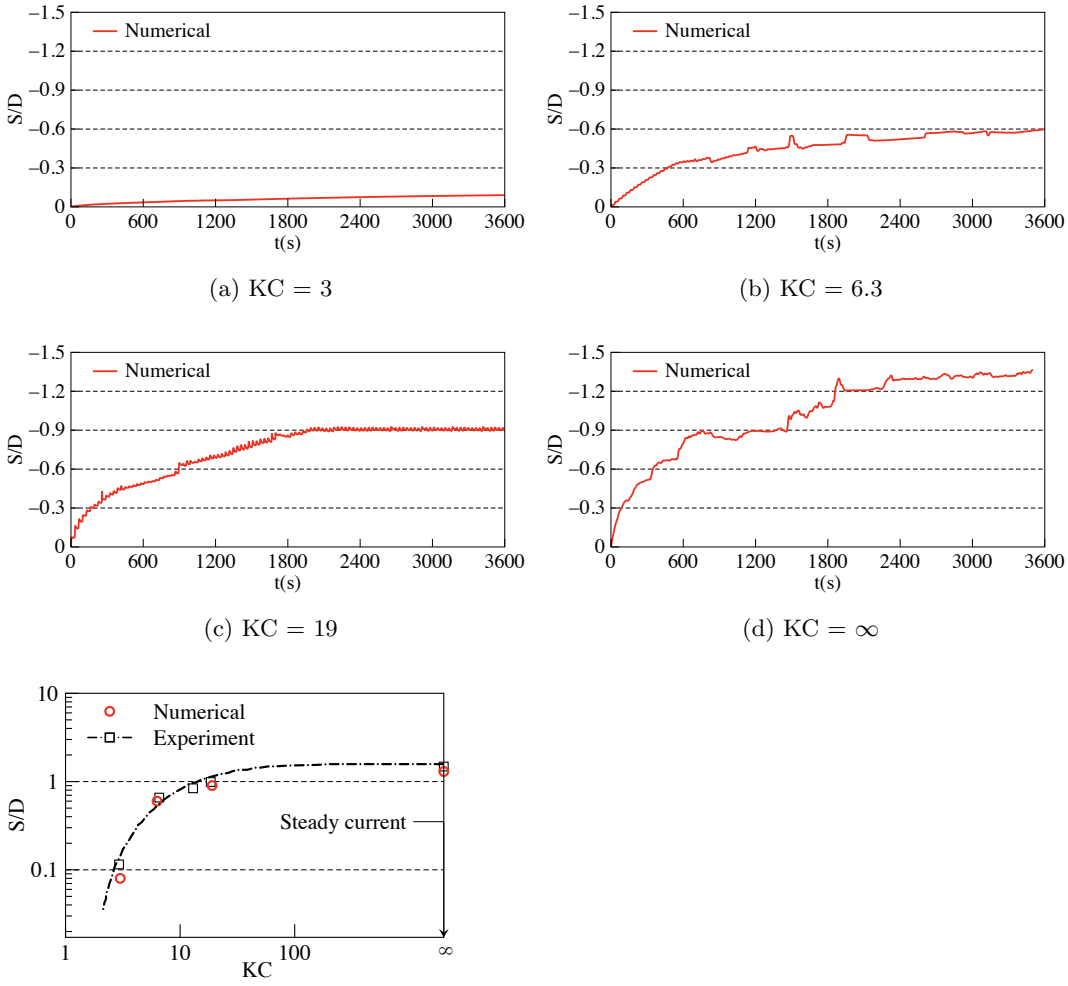

(a) KC = 3

(b) KC = 6.3

(c) KC = 19

(d) KC = ∞

(e) Variation of the S/D with KC

Figure 14: Temporal variation of the wave-induced scour depth and the change in the normalised maximum scour depth S/D and with KC, $G/D = 0.4$. The red solid line shows the simulated temporal variation of wave-induced scour, the red circles are the normalised maximum scour depth and the black squares with the dotted line are the experimental result (Sumer and Fredsøe, 1998).

In addition, the magnitude of local wave scour peaks, i.e. the instantaneous increase in

the scour during the wave crest action and the maximum scour depth (S/D) are found to increase with the KC number. This is because higher wave activity at higher KC numbers lead to the development of larger bed shear stresses at the bed and the formation of a deeper scour hole. Fig. 14(e) shows the variation of the normalised maximum scour depth S/D as KC increases for $G/D = 0.4$. The result shows that the initial growth of the normalised maximum scour depth S/D is quite high. The increase in S/D seems to increase by a factor of 10 as KC changes from KC = 3 to KC =19. The maximum scour depth for KC = ∞ is found to be $S/D = 1.3$ which seems slightly lower compared to the experimental data. Apart from this difference, the simulated results are found to be consistent with the experimental data (Sumer and Fredsøe, 1998) as clearly shown in Fig. 14(e).

5 Summary and Conclusions

The open-source CFD model REEF3D is used for the numerical modelling of wave-induced scour around the piles in a side-by-side arrangement. The model solves the three-dimensional RANS-equations, together with a $k-\omega$ turbulence model. The simulated wave flow is coupled to the morphological module of the REEF3D to investigate the wave-induced scour around piles. The wave generation and the wave-induced scour are validated by comparison to wave theory and experimental data, respectively. First, a full-sized 2D NWT without a sediment bed of $L = 28$ m is simulated for the wave generation with the relaxation method and the wave absorption using the AWA method. Then, another simulation is conducted in a reduced-length 2D NWT of $L = 4.4$ m using the AWA method for both the wave generation and absorption. It is found that the quality of the waves generated in a full-sized NWT and in a reduced-length NWT are the same.

The model is subsequently tested for scour calculations in a full-sized and reduced-length 3D NWT. The first simulation is carried out in a full-sized NWT of $L = 28$ m. Then, the other simulation is run by reducing the NWT length to $L = 4.4$ m. It is found that results of the scour calculations are almost the same for both the full-sized and the reduced-length NWT. A small disagreement is seen between the numerical and the experimental results due to the use of wall functions to determine the bed shear stress at the solid boundary. In addition, the model is tested for the partial temporal decoupling of the time scales of the morphological and hydrodynamic models. In these tests, the equilibrium scour is achieved by imposing a different number of waves with a reduction of DF values. It is found that similar to the full-sized NWT, a developed wave field and the resulting scouring process can be simulated in a reduced-length NWT without compromising the wave quality or the local scour physics. Additionally, the partial temporal decoupling of the time scales of the morphological and hydrodynamic models is a viable way to simulate the maximum scour depth with an optimized flow simulation time, which further reduces the CPU requirement for the scouring process calculation.

Finally, the validated model is used for the simulation of the scouring process around piles in a side-by-side arrangement. The wave hydrodynamics are discussed in order to investigate the jet effect between the two piles as G/D increases. It is found that when the wave front hits the piles, the horizontal velocity increases while the vertical velocity decreases. The combined effect of the change in the horizontal and the vertical velocities is to enhance the jet effect. The impact of the jet effect is further investigated for the variation in the normalised maximum scour depth S/D with G/D. The simulated S/D is found to increase for G/D = 0 to 0.3 and decreases then for G/D = 0.3 to 2 and no scour is observed between the two piles for $G/D > 2$. The results are confirmed by the study carried out by Sumer and Fredsøe (1998), which suggests that for $G/D > 2$, piles in a side-by-side arrangement act as individual piles with two distinct scour holes. It appears that S/D increases with the KC number $G/D = 0.4$. Overall, the the numerical model REEF3D shows a good performance for the simulation of the wave-induced scour, resolving the detailed hydrodynamics around the piles and its interaction with the sediment transport processes.

Acknowledgements

This study has been carried out under the POL- NOR/200336/95/2014 and the authors are grateful to the grants provided by the Research Council of Norway and the National Center for Research and Development in Poland. This study was supported in part with computational resources at the Norwegian University of Science and Technology (NTNU) provided by NOTUR, http://www.notur.no.

References

References

Afzal, M.S., Bihs, H., Kamath, A. and Arntsen, Ø.A. (2015). Three-dimensional numerical modeling of pier scour under current and waves using level-set method. *Journal of Offshore Mechanics and Arctic Engineering*, **137**(3), 032001.

Ahmad, N., Afzal, S., Bihs, H. and Arntsen, Ø.A. (2015). Three-dimensional numerical modeling of local scour around a non-slender cylinder under varying wave conditions. In: *36th IAHR World Congress, June 2015, The Netherlands.*

Alagan Chella, M., Bihs, H., Myrhaug, D. and Muskulus, M. (2016). Hydrodynamic characteristics and geometric properties of plunging and spilling breakers over impermeable slopes. *Ocean Modelling*, **103**, 53–72.

Ashby, S.F. and Flagout, R.D. (1996). A parallel mulitgrid preconditioned conjugate gradient algorithm for groundwater flow simulations. *Nuclear Science and Engineering*, **124**(1), 145–159.

Baykal, C., Sumer, B.M., Fuhrman, D.R., Jacobsen, N.G. and Fredsøe, J. (2015). Numerical investigation of flow and scour around a vertical circular cylinder. *Phil. Trans. R. Soc. A*, **373**(2033), 20140104.

Baykal, C., Sumer, B.M., Fuhrman, D.R., Jacobsen, N.G. and Fredsøe, J. (2017). Numerical simulation of scour and backfilling processes around a circular pile in waves. *Coastal Engineering*, **122**(Supplement C), 87 – 107. ISSN 0378-3839.

Bayram, A. and Larson, M. (2000). Analysis of scour around a group of vertical piles in the field. *Journal of Waterway, Port, Coastal, and Ocean Engineering*, **126**, 215–220.

Berthelsen, P.A. and Faltinsen, O.M. (2008). A local directional ghost cell approach for incompressible viscous flow problems with irregular boundaries. *Journal of Computational Physics*, **227**, 4354–4397.

Bihs, H. and Kamath, A. (2017). A combined level set/ghost cell immersed boundary representation for floating body simulations. *International Journal for Numerical Methods in Fluids*, **83**(12), 905–916.

Bihs, H., Kamath, A., Alagan Chella, M., Aggarwal, A. and Arntsen, Ø.A. (2016). A new level set numerical wave tank with improved density interpolation for complex wave hydrodynamics. *Computers & Fluids*, **140**, 191–208.

Bihs, H. and Olsen, N.R.B. (2011). Numerical modeling of abutment scour with the focus on the incipient motion on sloping beds. *Journal of Hydraulic Engineering*, **137**(10), 1287–1292.

Breuer, M., Bernsdorf, J., Zeiser, T. and Durst, F. (2000). Accurate computations of the laminar flow past a square cylinder based on two different methods: lattice-boltzmann and finite-volume. *International Journal of Heat and Fluid Flow*, **21**(2), 186 – 196. ISSN 0142-727X.

Burkow, M. and Griebel, M. (2016). A full three dimensional numerical simulation of the sediment transport and the scouring at a rectangular obstacle. *Computers & Fluids*, **125**, 1–10.

Chorin, A. (1968). Numerical solution of the Navier-Stokes equations. *Mathematics of Computation*, **22**, 745–762.

Chow, W. and Herbich, J. (1978). Scour around a group of piles. In: *Proc. Offshore Technol. Paper No. 3308, Dallas, Tex.*

Dey, S. (2003). Threshold of sediment motion on combined transverse and longitudinal sloping beds. *Journal of Hydraulic Research*, **41**(4), 405–415.

Durbin, P.A. (2009). Limiters and wall treatments in applied turbulence modeling. *Fluid Dynamics Research*, **41**, 1–18.

Griebel, M., Dornseifer, T. and Neunhoeffer, T. (1998). *Numerical simulation in fluid dynamics: a practical introduction*. SIAM.

Hunt, J.N. (1954). The turbulent transport of suspended sediment in open channels. In: *Proceedings of the Royal Society of London A: Mathematical, Physical and Engineering Sciences*, volume 224, 322–335. The Royal Society.

Jacobsen, N.G., Fuhrman, D.R. and Fredsøe, J. (2012). A wave generation toolbox for the open-source CFD library: Openfoam. *International Journal for Numerical Methods in Fluids*, **70**(9), 1073–1088.

Jiang, G.S. and Peng, D. (2000). Weighted ENO schemes for Hamilton-Jacobi equations. *SIAM Journal on Scientific Computing*, **21**, 2126–2143.

Jiang, G.S. and Shu, C.W. (1996). Efficient implementation of weighted ENO schemes. *Journal of Computational Physics*, **126**, 202–228.

Kamath, A., Alagan Chella, M., Bihs, H. and Arntsen, Ø.A. (2016). Breaking wave interaction with a vertical cylinder and the effect of breaker location. *Ocean Engineering*, **128**, 105 – 115.

Kovacs, A. and Parker, G. (1994). A new vectorial bedload formulation and its application to the time evolution of straight river channels. *Journal of Fluid Mechanics*, **267**, 153–183.

Liu, X. and Garcia, M. (2008). Three-dimensional numerical model with free water surface and mesh deformation for local sediment scour. *Journal of Waterway, Port, Coastal and Ocean Engineering*, **134**(4), 203–217.

Lysne, D. (1970). *Movement of Sand in Tunnels*. River and Harbour Laboratory at The Technical University of Norway. River and Harbour Laboratory at The Technical University of Norway.

Melville, B.W. and Coleman, S.E. (2000). *Bridge scour*. Highlands Ranch, Colo. : Water Resources Publications, LLC. ISBN 1887201181 (pbk.).

Myrhaug, D. and Rue, H. (2005). Scour around group of slender vertical piles in random waves. *Applied Ocean Research*, **27**, 56–63.

Nelson, J.M., Bennett, J.P. and Wiele, S.M. (2005). *Flow and Sediment-Transport Modeling*, 539–576. ISBN 9780470868331.

Nielsen, A.W., Sumer, B.M., Ebbe, S.S. and Fredsøe, J. (2012). Experimental study on the scour around a monopile in breaking waves. *Journal of Waterway, Port, Coastal, and Ocean Engineering*, **138**(6), 501–506. 10.1016/j.coastaleng.2018.04.01610.1061/(ASCE)WW.1943-5460.0000148.

Olsen, N.R.B. (2003). Three-dimensional cfd modeling of self-forming meandering channel. *Journal of Hydraulic Engineering*, **129**(5), 366–372.

Olsen, N.R.B. and Kjellesvig, H.M. (1998). Three-dimensional numerical flow modelling for estimation of maximum local scour depth. *IAHR Journal of Hydraulic Research*, **36**(4), 579–590.

Olsen, N.R.B. and Melaaen, M.C. (1993). Three-dimensional calculation of scour around cylinders. *Journal of Hydraulic Engineering*, **119**(9), 1048–1054.

Osher, S. and Sethian, J.A. (1988). Fronts propagating with curvature-dependent speed: algorithms based on Hamilton-Jacobi formulations. *Journal of Computational Physics*, **79**, 12–49.

Peng, D., Merriman, B., Osher, S., Zhao, H. and Kang, M. (1999). A PDE-based fast local level set method. *Journal of Computational Physics*, **155**, 410–438.

Posey, C.J. (1961). Erosion protection of production structures. In: *Proc., 9th Congress of IAHR, September-1961, Dubrovnik, Yugoslavia*, 1157–1162.

Richardson, J. and Panchang, V. (1998). Three-dimensional simulation of scour inducing flow at bridge piers. *Journal of Hydraulic Engineering*, **124**(5), 530–540.

Roulund, A., Sumer, B.M., Fredsøe, J. and Michelsen, J. (2005). Numerical and experimental investigation of flow and scour around a circular pier. *Journal of Fluid Mechanics*, **534**, 351–401.

Rouse, H. (1937). Modern conceptions of the mechanics of turbulence. *Trans. ASCE*, **102**, 463–543.

Schäffer, H.A. and Klopman, G. (2000). Review of multidirectional active wave absorption methods. *Journal of Waterway, Port, Coastal, and Ocean Engineering*, **126**(2), 88–97.

Shu, C.W. and Osher, S. (1988). Efficient implementation of essentially non-oscillatory shock capturing schemes. *Journal of Computational Physics*, **77**, 439–471.

Sumer, B. and Fredsøe, J. (2002). *Mechanics of Scour in Marine Environment.* World Scientific Publishing Co. Pte. Ltd.

Sumer, B.M. and Fredsøe, J. (1998). Wave scour around group of vertical piles. *Journal of Waterway, Port, Coastal, and Ocean Engineering*, **124**(5), 248–256.

Sumer, B.M. and Fredsøe, J. (2001). Wave scour around a large vertical circular cylinder. *Journal of Waterway, Port, Coastal, and Ocean Engineering*, **127**(3), 125–134.

Sumer, B.M., Fredsøe, J. and Niels, K. (1992). Scour around verticle piles in waves. *Journal of Waterway, Port, Coastal, and Ocean Engineering*, **118**(1), 15–31.

Tseng, M., Yen, C. and Song, C. (2000). Computation of three-dimensional flow around square and circular bridge piers. *International Journal for Numerical Methods in fluids*, **34**, 207–227.

van Rijn, L.C. (1984*a*). Sediment transport, part I: Bed load transport. *Journal of Hydraulic Engineering*, **110**(10), 1431–1456.

van Rijn, L.C. (1984*b*). Sediment transport, part II: Suspended load transport. *Journal of Hydraulic Engineering*, **110**(11), 1613–1641.

Vorst, H.v. (1992). BiCGStab: A fast and smoothly converging variant of Bi-CG for the solution of nonsymmetric linear systems. *SIAM Journal on Scientific and Statistical Computing*, **13**, 631–644.

Whitehouse, R.J.S. (1998). *Scour at marine structures: A manual for practical applications.* Thomas Telford.

Wilcox, D.C. (1994). *Turbulence modeling for CFD.* DCW Industries Inc., La Canada, California.

Wu, W., Rodi, W. and Wenka, T. (2000). 3D numerical modeling of flow and sediment transport in open channels. *Journal of Hydraulic Engineering*, **126**(1), 4–15.

Notations

The following symbols are used in this paper:

α = transverse bed slope;
φ = angle of repose;
η = ratio of the drag force to the inertia force;
τ = bed shear stress;
τ_0 = Shields critical bed shear stress;
τ_{cr} = modified critical bed stress;
$\widetilde{\tau}$ = critical bed shear stress ratio;
ρ = fluid density;
ρ_s = sediment density;
ν = fluid kinematic viscosity;
ν_t = eddy viscosity;
ω = specific turbulent dissipation;
$\phi(\vec{x}, t)$ = level set function;
κ = von Karman constant;
$q_{b,i}$ = bed-load transport rate;
w_s = fall velocity of the sediment particles;
$\Gamma(x)$ = the relaxation function
Γ = sediment mixing coefficient;
θ = Shields parameter;
θ_c = critical Shields parameter;
λ = wavelength;
δ = wave discrepancy;
δ_{cr} = wave crests discrepancy;
δ_{tr} = wave troughs discrepancy;
δ_{ph} = wave phase discrepancy;
a = reference level;
d_{50} = median grain size;
g = gravitational acceleration;

i, j, k	=	indices representing directions along the x-, y- and z-axis;
k_s	=	equivalent sand roughness;
k	=	turbulent kinetic energy;
h	=	still water level;
n	=	sediment porosity;
η_r	=	reflected wave amplitude;
η_m	=	actual free surface elevation;
p	=	pressure;
s	=	specific density;
t	=	time;
u	=	horizontal velocity;
v	=	vertical velocity;
u_r	=	relative change in horizontal velocity;
w_r	=	relative change vertical velocity;
z	=	bed-level;
D	=	pile diameter (m);
DF	=	decoupling factor;
E	=	entrainment rate;
G	=	gap between two piles (m);
G/D	=	gap ratio;
H	=	wave height;
KC	=	Keulegan-Carpenter number;
NWT	=	numerical wave tank;
N	=	number of incident waves;
P_k	=	turbulent production rate;
S	=	maximum scour depth;
S/D	=	normalised maximum scour depth;